Downloaded from https://academic.oup.com/mnras/article/506/4/4914/6318873 by University of California, Santa Cruz user on 20 August 202:

Advance Access publication 2021 July 10

Modelling coexisting GSF and shear instabilities in rotating stars

Eonho Chang ¹,2★ and Pascale Garaud ★

- ¹Department of Applied Mathematics, Baskin School of Engineering, University of California, Santa Cruz, CA 95064, USA
- ²Graduate Interdisciplinary Program in Applied Mathematics, University of Arizona, Tucson, AZ 85721, USA

Accepted 2021 July 1. Received 2021 June 29; in original form 2021 May 20

ABSTRACT

Zahn's widely used model for turbulent mixing induced by rotational shear has recently been validated (with some caveats) in non-rotating shear flows. It is not clear, however, whether his model remains valid in the presence of rotation, even though this was its original purpose. Furthermore, new instabilities arise in rotating fluids, such as the Goldreich–Schubert–Fricke (GSF) instability. Which instability dominates when more than one can be excited, and how they influence each other, were open questions that this paper answers. To do so, we use direct numerical simulations of diffusive stratified shear flows in a rotating triply periodic Cartesian domain located at the equator of a star. We find that either the GSF instability or the shear instability tends to take over the other in controlling the system, suggesting that stellar evolution models only need to have a mixing prescription for each individual instability, together with a criterion to determine which one dominates. However, we also find that it is not always easy to predict which instability 'wins' for given input parameters, because the diffusive shear instability is subcritical, and only takes place if there is a finite-amplitude turbulence 'primer' to seed it. Interestingly, we find that the GSF instability can in some cases play the role of this primer, thereby providing a pathway to excite the subcritical shear instability. This can also drive relaxation oscillations, which may be observable. We conclude by proposing a new model for mixing in the equatorial regions of stellar radiative zones due to differential rotation.

Key words: hydrodynamics – instabilities – turbulence – stars: evolution.

1 INTRODUCTION

The theory of stellar evolution models the life of stars from their birth to their death, and is generally successful in reproducing most salient aspects of the Hertzsprung-Russel (HR) diagram. Discrepancies between model and observations, however, usually emerge when probing more specific aspects of stellar evolution using photospheric chemical abundances (see e.g. Pinsonneault 1997) or asteroseismology (see e.g. Aerts 2021), and are often resolved by invoking some amount of extra mixing in the star's radiative zone. There are many possible sources of extra mixing in stars, as discussed for instance by Zahn (1974). Of particular interest in recent years are the diffusive (alternatively called secular) shear instability (Zahn 1974, 1992; Prat & Ligniéres 2013, 2014; Garaud, Gallet & Bischoff 2015; Garaud & Kulenthirarajah 2016; Prat et al. 2016; Garaud, Gagnier & Verhoeven 2017; Gagnier & Garaud 2018), and the Goldreich-Schubert-Fricke (GSF) instability (Goldreich & Schubert 1967; Fricke 1968; Knobloch 1982; Knobloch & Spruit 1982; Korycansky 1991; Rashid, Jones & Tobias 2008; Barker, Jones & Tobias 2019, 2020), that can extract energy from the differential rotation of the star to drive turbulence, and therefore transport of chemical species and angular momentum. In what follows, we begin by briefly reviewing what is known about both types of instabilities and their transport properties, and then discuss what outstanding issues remain to be studied. We ignore magnetic fields, for simplicity,

but acknowledge that they would in practice form an important part of the complete story. Again for simplicity, we consider only the equatorial region of a star, noting that the non-equatorial case is substantially more complicated (Knobloch & Spruit 1982; Barker et al. 2020). Near the equator, by symmetry, the angular velocity Ω is a function of the radius r only, so that we can assume that $\Omega = \Omega(r)$.

1.1 Shear instabilities

It has long been known (Richardson 1920; Howard 1961; Miles 1961) that non-diffusive (adiabatic) shear instabilities only grow when the local Richardson number *J* drops below a constant of order unity somewhere in the flow, where

$$J = \frac{N^2}{S^2},\tag{1}$$

N is the Brunt–Väisälä frequency and S is the local shear (which would be equal to $S = S_{\Omega} = r d\Omega/dr$ for rotational shear). The criterion has a simple energetic interpretation: for instability to occur, the kinetic energy extracted by the perturbations from the mean flow, which is proportional to S^2 , must exceed the potential energy lost in mixing the stratified fluid, which is proportional to N^2 . In practice, however, this criterion is rarely satisfied (see Garaud 2021, for a simple explanation), except very close to the edge of a convective region where $N \to 0$. As such, standard adiabatic shear instabilities are almost never excited in radiation zones.

^{*} E-mail: eonhochang@math.arizona.edu (EC); pgaraud@ucsc.edu (PG)

Crucially, Townsend (1958) noted that the Richardson criterion is relaxed by non-adiabatic effects, because the stabilizing role of thermal stratification is reduced by the fluid parcel exchanging heat with its surroundings. Adapting Townsend's results, Zahn (1974) proposed a modified criterion for diffusive shear instabilities applicable to optically thick stellar interiors. This criterion states that shear-induced turbulence can be sustained provided

$$JPr < (JPr)_{c},$$
 (2)

where $(JPr)_c$ is a constant he argues must be of the order of 10^{-3} , and $Pr = \nu/\kappa_T$ is the Prandtl number, defined as the ratio of the kinematic viscosity ν and the thermal diffusivity κ_T . Noting that $Pr \sim 10^{-5}$ – 10^{-9} in typical stellar interiors (Garaud 2021), Zahn's criterion suggests that flows with $J \sim 10^2$ – 10^6 would be unstable, which is within the range of expected Richardson numbers in stars (although some have much larger Richardson numbers still). Zahn (1992) later derived a turbulent mixing coefficient resulting from these diffusive stratified shear instabilities, which can in principle be used to model both chemical transport (D_{turb}) or momentum transport (D_{turb}):

$$D_{\rm turb} \simeq \nu_{\rm turb} = C \frac{\kappa_{\rm T}}{I},$$
 (3)

where C is a constant of order unity.

The two components of Zahn's turbulent mixing prescription, namely equations (2) and (3), have been tested against direct numerical simulations (DNS), and found to be valid, in certain limits, for *non-rotating* diffusive shear flows (see in particular Prat et al. 2016; Garaud et al. 2017). Both studies found that Zahn's stability criterion applies with $(JPr)_c \approx 0.007$. They also found that (3) is correct for diffusive shear flows, but only as long as the turbulence is local, and $JPr \ll (JPr)_c$. A modified version of the mixing prescription that takes both issues into account was recently proposed by Garaud et al. (2017), and is discussed in more detail in Section 6.2. Testing the validity of Zahn's model for rotating shear flows, which was its intended purpose (and the way it is commonly used in stellar evolution codes) is one of the goals of this paper.

Finally, note that a key aspect of diffusive shear instabilities is that they are not linearly excited when $J\gg 1$, but instead, emerge through non-linear (subcritical) instabilities (see e.g. Garaud et al. 2015; Garaud & Kulenthirarajah 2016). As such, they are subject to hysteresis (see Gagnier & Garaud 2018), and are only excited in this subcritical regime provided a minimum amount of turbulence is already present in the system to 'prime' the instability. This, to our knowledge, is not accounted for in any stellar evolution code.

1.2 Adding rotation: the GSF instability

Although Zahn himself suggested that the results he derived for non-rotating shear flows might be directly applied to flows with rotational shear (Zahn 1992), it is not obvious as there are several complications caused by rotation. First, it can influence the dynamics of the shear instability itself, by constraining the turbulence to be progressively more invariant along the rotation axis as the rotation rate increases (Gallet 2015). Secondly, it is known to drive centrifugal instabilities, which ultimately extract energy from the angular momentum gradient rather than from the shear, and are therefore distinct from shear instabilities (Rayleigh 1917; Solberg 1936; Høiland & Bjerknes 1939; Høiland 1941). In the absence of viscosity and thermal diffusion, and in the equatorial region of a star (which we are concerned with in this paper), the so-called Solberg—Høiland criterion for centrifugal instability in differentially rotating,

stratified shear flows, reads

$$\frac{1}{r^3}\frac{\partial}{\partial r}(r^4\Omega^2) + N^2 = 2\Omega(2\Omega + S_{\Omega}) + N^2 \le 0 \tag{4}$$

in the notation introduced above. In the absence of stratification $(N^2=0)$, this criterion recovers the well-known Rayleigh instability criterion for centrifugal instabilities (Rayleigh 1917), which states that angular momentum must decrease outward for instability to occur. As such, the instability can only be excited when S_{Ω} is sufficiently negative. In a radiative zone $(N^2>0)$, the thermal stratification acts to stabilize the flow as expected. In most stars, this would be sufficient to suppress centrifugal instabilities altogether, were it not – as in the case of shear instabilities – for non-adiabatic effects.

Indeed, Goldreich & Schubert (1967) and Fricke (1968) demonstrated that taking into account the effects of thermal diffusion greatly relaxes the instability criterion, which now reads

$$\frac{1}{r^3}\frac{\partial}{\partial r}(r^4\Omega^2) + \frac{\nu}{\kappa_{\rm T}}N^2 = 2\Omega(2\Omega + S_{\Omega}) + \Pr(N^2 \le 0,$$
 (5)

in the equatorial region of a star. Since $Pr \ll 1$, this criterion is much more easily satisfied than (4). The instabilities that arise in that case are now known as GSF instabilities.

Goldreich & Schubert (1967) immediately noticed the strong similarity between the GSF instability and the double-diffusive fingering instability (see also Barker et al. 2019, for a detailed comparison of the two). Indeed, the fingering instability exists in fluids that have a stable thermal stratification and an unstable compositional stratification. On sufficiently small scales, thermal diffusion reduces the stabilizing role of the temperature gradient, enabling perturbations to draw energy from the unstable composition gradient. Similarly in the case of the GSF instability, thermal diffusion enables small-scale perturbations to extract energy from the unstable angular momentum gradient. In both cases, a sensible scale for the instability is

$$d = \left(\frac{\kappa_{\rm T} \nu}{N^2}\right)^{1/4},\tag{6}$$

where we note that the fastest-growing modes can take a larger or smaller value than d depending on the parameters (see e.g. the appendix of Barker et al. 2020). The unstable region of parameter space can be written as

$$1 \le R_0 \le \frac{\kappa_{\rm U}}{\kappa_{\rm T}},\tag{7}$$

where $\kappa_{\rm U}$ is the diffusivity associated with the unstable field (i.e. the compositional diffusivity in the fingering case, and the kinematic viscosity in the GSF case), and R_0 is a non-dimensional ratio of the square of time-scales associated with the stabilizing and destabilizing stratifying components, respectively:

$$R_0 = -\frac{N^2}{N_C^2} \text{ in the fingering case,}$$
 (8)

$$R_0 = -\frac{N^2}{2\Omega(2\Omega + S_{\Omega})} \text{ in the GSF case,}$$
 (9)

where N_C^2 is the square of the buoyancy frequency associated with the composition gradient (which is negative when the latter is unstably stratified), and $2\Omega(2\Omega + S_\Omega)$ is the square of the epicyclic frequency associated with the angular momentum gradient (which is again negative when the latter is unstably stratified). In fact, the similarity between the two systems is so strong that they are exactly analogous in two dimensions, under an appropriate change of variables (see a nice exposition of this analogy by Barker et al. 2019). As a result,

4916 E. Chang and P. Garaud

many of the results recently obtained in the fingering context (see the reviews by Garaud 2018, 2020a) apply in the GSF case. Notably, it is possible to derive approximate analytical expressions for the growth rate of the GSF instability at low Prandtl number (following the work of Brown, Garaud & Stellmach 2013), and to construct a model for turbulent momentum transport that fits the data from DNS remarkably well for a wide range of parameters (Barker et al. 2019). This model can be written as

$$\nu_{\text{turb}} = \frac{C_B^2}{S_\Omega} \frac{S_\Omega + 2\Omega}{\lambda + \nu k^2} \frac{\lambda^2}{k^2},\tag{10}$$

when (7) is satisfied, where λ and k are the growth rate and wavenumber of the fastest-growing GSF modes, respectively, and C_B is a universal constant that is fitted to the data (see more on this in Section 6.4). The constant C_B is related to the constant A in Barker et al. (2019), see their equation (31), as $C_B^2 = A^2/2$.

1.3 Coexistence of shear and GSF instabilities

From the respective criteria for diffusive shear instabilities and GSF instabilities, we see that an interesting situation can arise when $S_{\Omega} < 0$, in which both instabilities are excited at the same time. In stellar evolution codes such as MESA (Paxton et al. 2011), this situation is usually dealt with by computing a mixing coefficient for each instability, and adding them together to obtain a 'total' mixing coefficient. However, this general practice is considered heretical by most fluid dynamicists, as there is a wealth of evidence showing that doing this often gives nonsensical results. For example, adding shear to convection or fingering convection can reduce mixing considerably (Garaud, Kumar & Sridhar 2019; Blass et al. 2021) instead of increasing it. There are also well-known cases in which two processes that would normally be stable, when taken individually, become unstable when they interact (Hughes & Weiss 1995; Radko 2016).

Based on these examples, one may naturally ask the question of what *really* happens when shear instabilities coexist with GSF instabilities. Of course, one may argue that by contrast with the examples cited above, the presence of shear is accounted for in the GSF instability criterion. However, the latter is a local model, which ignores the possibility of global shearing modes. In addition, it also ignores the contribution of the subcritical branch of diffusive shear instabilities. Conversely, the shear instability model ignores rotation entirely, but the latter could affect both the instability criterion, and the mixing model. As such it is important to revisit the problem of diffusive instabilities in rotating, stratified shear flows, and see whether the existing mixing models described above apply or not.

We begin by presenting the model set-up used in this paper in Section 2. In Section 3, we perform a linear stability analysis of the model system, and demonstrate the existence of coexisting instabilities in Section 4. In Section 5, we present some qualitative results of the numerical investigation, while Section 6 studies them more quantitatively by comparing the measured mixing coefficients with the models of Garaud et al. (2017) and Barker et al. (2019). This section will also reveal some of the more unusual aspects of the interaction between shear and GSF instabilities. Finally, Section 7 summarizes our results, and discusses their implications for stellar evolution models.

2 MODEL SET-UP

We consider a Cartesian domain located at the equator of a star, rotating with a constant angular velocity $\Omega = \Omega_0 \hat{e}_z$. The unit vectors

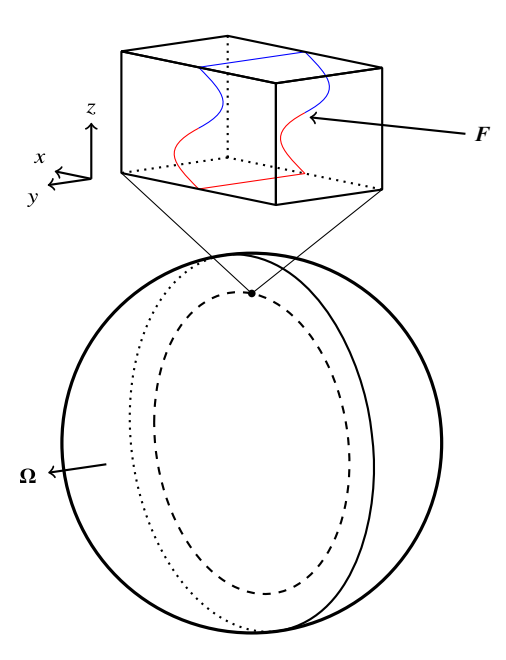


Figure 1. Model geometry. An imposed sinusoidal body force F drives an equatorial mean flow in the azimuthal direction, which varies with z but is invariant in y.

 $(\hat{\boldsymbol{e}}_x, \hat{\boldsymbol{e}}_y, \hat{\boldsymbol{e}}_z)$ are chosen such that $\hat{\boldsymbol{e}}_y$ points in the direction of Ω , $\hat{\boldsymbol{e}}_z$ points in the direction of $-\boldsymbol{g}$ (where \boldsymbol{g} is gravity), and $\hat{\boldsymbol{e}}_x$ is in the azimuthal direction and is chosen so that the system right-handed (see Fig. 1).

The domain is assumed to be located in a radiative zone, which is therefore stably stratified in terms of the potential temperature. We ignore for simplicity the possibility of a compositional stratification. Assuming that the domain size is smaller than any of the local scale heights, we use the Boussinesq approximation (Spiegel & Veronis 1960). Consistent with this approximation, we use a linear background thermal stratification in the z direction as $T_0(z) = T_m + zT_{0z}$, where T_m and T_{0z} are constant. Perturbations to this background are assumed to be periodic in all three directions. Finally, we assume the presence of a body force of the form $F = F_0 \sin(k_s z) \hat{e}_x$, of amplitude F_0 and wavenumber k_s , which drives an azimuthal flow (see Fig. 1).

The following dimensional equations govern the dynamics of the model described above:

$$\rho_{\rm m} \left(\frac{\partial \mathbf{u}}{\partial t} + \mathbf{u} \cdot \nabla \mathbf{u} + 2\mathbf{\Omega} \times \mathbf{u} \right) = -\nabla p + \rho \mathbf{g} + \rho_{\rm m} \nu \nabla^2 \mathbf{u}
+ F_0 \sin(k_s z) \hat{\mathbf{e}}_x,
\frac{\partial T}{\partial t} + \mathbf{u} \cdot \nabla T + w \left(T_{0z} - \frac{\mathrm{d} T_{\rm ad}}{\mathrm{d} z} \right) = \kappa_{\rm T} \nabla^2 T,
\nabla \cdot \mathbf{u} = 0,
\frac{\rho}{\rho_{\rm m}} = -\alpha T,$$
(11)

where ρ , p, and T are the density, pressure, and temperature perturbations away from hydrostatic equilibrium, $\rho_{\rm m}$ is the mean density of the region considered, and ${\bf u}=(u,v,w)$ is the velocity field. We assume the kinematic viscosity v, thermal diffusivity $\kappa_{\rm T}$, the local gravity g, and the thermal expansion coefficient $\alpha=-\rho_{\rm m}^{-1}(\partial\rho/\partial T)$ to be constant. The adiabatic temperature gradient is ${\rm d}T_{\rm ad}/{\rm d}z=-g/c_{\rm p}$, where $c_{\rm p}$ is the specific heat at constant pressure.

Because of the imposed sinusoidal forcing, the system has a laminar steady-state solution given by

$$\boldsymbol{u}_L = \frac{F_0}{\rho_{\rm m} \nu k_s^2} \sin(k_s z) \hat{\boldsymbol{e}}_x. \tag{12}$$

We can non-dimensionalize the governing equations using the amplitude of the laminar solution $U_L = F_0/(\rho_{\rm m}\nu k_s^2)$ as a velocity scale and the spatial scale of the laminar solution k_s^{-1} as a length-scale [and thus define $t_s = (k_s U_L)^{-1}$ as a time-scale]. The corresponding non-dimensional equations are

$$\frac{\mathrm{D}\hat{\boldsymbol{u}}}{\mathrm{D}\hat{\boldsymbol{t}}} = -\nabla\hat{\boldsymbol{p}} + \mathrm{Ri}\hat{\boldsymbol{T}}\hat{\boldsymbol{e}}_z + \frac{1}{\mathrm{Re}}\nabla^2\hat{\boldsymbol{u}} - \frac{\hat{\boldsymbol{w}}}{\mathrm{Ro}}\hat{\boldsymbol{e}}_x + \frac{\hat{\boldsymbol{u}}}{\mathrm{Ro}}\hat{\boldsymbol{e}}_z + \frac{1}{\mathrm{Re}}\sin\hat{\boldsymbol{z}}\hat{\boldsymbol{e}}_x,
\frac{\partial\hat{T}}{\partial\hat{\boldsymbol{t}}} + \hat{\boldsymbol{u}} \cdot \nabla\hat{T} + \hat{\boldsymbol{w}} = \frac{1}{\mathrm{Pe}}\nabla^2\hat{T},
\nabla \cdot \hat{\boldsymbol{u}} = 0,$$
(13)

where hats denote non-dimensional variables (and the gradient operators are now implicitly non-dimensional), with the following dimensionless parameters:

$$Re = \frac{U_L}{k_s \nu} = \frac{F_0}{\rho_m \nu^2 k_s^3}, \quad Ri = \frac{N^2}{U_L^2 k_s^2} = \frac{\alpha g T_{0z} \rho_m^2 \nu^2 k_s^2}{F_0^2},$$

$$Pe = \frac{U_L}{k_s \kappa_T} = \frac{F_0}{\rho_m \kappa_T \nu k_s^3} = PrRe, \quad Ro = \frac{k_s U_L}{2\Omega_0} = \frac{F_0}{2\Omega_0 \rho_m \nu k_s}.$$
(14)

The Reynolds number Re quantifies the ratio of the laminar flow shearing rate to the viscous diffusion rate across a length-scale k_s^{-1} . The Richardson number Ri is the square of the ratio of the buoyancy frequency to the laminar flow shearing rate, which is used as a proxy for quantifying the potential energy lost in mixing the stratification to the kinetic energy gained from the shear. The Péclet number Pe is the ratio of the laminar flow shearing rate to the thermal diffusion rate. Finally, the Rossby number Ro is the ratio of the laminar flow shearing rate to the rotation rate, which measures the relative importance of the inertial terms and the Coriolis force.

3 LINEAR STABILITY ANALYSIS

3.1 Linearized equations

In this section, we look at the stability of the laminar steady-state solution. We consider 3D infinitesimal perturbations (denoted by the primes) such that $\hat{\boldsymbol{u}} = \hat{\boldsymbol{u}}_L + \hat{\boldsymbol{u}}'$, where $\hat{u}_L(\hat{z}) = \sin \hat{z}$. When expanded in component form, the linearization of the system of equations (13) results in :

$$\begin{split} \frac{\partial \hat{u}'}{\partial \hat{t}} + \hat{w}' \frac{\mathrm{d}\hat{u}_L}{\mathrm{d}\hat{z}} + \hat{u}_L \frac{\partial \hat{u}'}{\partial \hat{x}} &= -\frac{\partial \hat{p}'}{\partial \hat{x}} + \frac{1}{\mathrm{Re}} \nabla^2 \hat{u}' - \frac{\hat{w}'}{\mathrm{Ro}}, \\ \frac{\partial \hat{v}'}{\partial \hat{t}} + \hat{u}_L \frac{\partial \hat{v}'}{\partial \hat{x}} &= -\frac{\partial \hat{p}'}{\partial \hat{y}} + \frac{1}{\mathrm{Re}} \nabla^2 \hat{v}', \\ \frac{\partial \hat{w}'}{\partial \hat{t}} + \hat{u}_L \frac{\partial \hat{w}'}{\partial \hat{x}} &= -\frac{\partial \hat{p}'}{\partial \hat{z}} + \mathrm{Ri} \hat{T}' + \frac{1}{\mathrm{Re}} \nabla^2 \hat{w}' + \frac{\hat{u}'}{\mathrm{Ro}}, \\ \frac{\partial \hat{T}'}{\partial \hat{t}} + \hat{u}_L \frac{\partial \hat{T}'}{\partial \hat{x}} + \hat{w}' &= \frac{1}{\mathrm{Pe}} \nabla^2 \hat{T}', \\ \frac{\partial \hat{u}'}{\partial \hat{x}} + \frac{\partial \hat{v}'}{\partial \hat{y}} + \frac{\partial \hat{w}'}{\partial \hat{z}} &= 0. \end{split} \tag{15}$$

where all primed quantities are assumed to be small.

This system of partial differential equations (PDEs) has nonconstant coefficients, since the function \hat{u}_L and its derivative are functions of \hat{z} . Nevertheless, we can use the periodicity of $\hat{u}_L(\hat{z})$ to transform it into a system of linear algebraic equations. We do so first by assuming that the perturbations $\hat{q}'(\hat{x}, \hat{y}, \hat{z}, \hat{t})$ (where \hat{q}' can be either u', \hat{T}' , or \hat{p}') can be written as normal modes of the form:

$$\hat{q}'(\hat{x}, \hat{y}, \hat{z}, \hat{t}) = \tilde{q}(\hat{z}) \exp(i\hat{k}_x \hat{x} + i\hat{k}_y \hat{y} + \hat{\lambda}\hat{t}), \tag{16}$$

where \hat{k}_x and \hat{k}_y are the non-dimensional wavenumbers in \hat{x} and \hat{y} , respectively, and $\hat{\lambda}$ is a non-dimensional complex growth rate. We seek solutions of the same periodicity as $\hat{u}_L(\hat{z})$, satisfying:

$$\tilde{q}(\hat{z}) = \sum_{n=-\infty}^{\infty} q_n \exp(in\hat{z}). \tag{17}$$

In practice, we limit the sum to a finite number of modes, ranging from n = -N to n = N. We found N = 20 to be sufficient and used this value throughout.

Substituting these ansätze into the linearized equations, we obtain a system of algebraic equations for the Fourier coefficients q_n , for n = -N to n = N (with the convention that the coefficients of modes with n < -N and n > N are set to zero):

$$\begin{split} \hat{\lambda}u_{n} + \frac{w_{n-1}}{2} + \frac{w_{n+1}}{2} + \frac{\hat{k}_{x}u_{n-1}}{2} - \frac{\hat{k}_{x}u_{n+1}}{2} \\ &= -i\hat{k}_{x}p_{n} - \operatorname{Re}^{-1}|\hat{k}_{n}|^{2}u_{n} - \operatorname{Ro}^{-1}w_{n}, \\ \hat{\lambda}v_{n} + \frac{\hat{k}_{x}v_{n-1}}{2} - \frac{\hat{k}_{x}v_{n+1}}{2} &= -i\hat{k}_{y}p_{n} - \operatorname{Re}^{-1}|\hat{k}_{n}|^{2}v_{n}, \\ \hat{\lambda}w_{n} + \frac{\hat{k}_{x}w_{n-1}}{2} - \frac{\hat{k}_{x}w_{n+1}}{2} &= -inp_{n} + \operatorname{Ri}T_{n} - \operatorname{Re}^{-1}|\hat{k}_{n}|^{2}w_{n} + \operatorname{Ro}^{-1}u_{n}, \\ \hat{\lambda}T_{n} + \frac{\hat{k}_{x}T_{n-1}}{2} - \frac{\hat{k}_{x}T_{n+1}}{2} + w_{n} &= -\operatorname{Pe}^{-1}|\hat{k}_{n}|^{2}T_{n}, \\ \hat{k}_{x}u_{n} + \hat{k}_{y}v_{n} + nw_{n} &= 0, \end{split}$$

where $\hat{k}_n = (\hat{k}_x, \hat{k}_y, n)$. The dimension of the system can be reduced by eliminating the pressure p_n analytically, resulting in

$$\hat{\lambda}u_{n} + \frac{w_{n-1}}{2} + \frac{w_{n+1}}{2} + \frac{\hat{k}_{x}u_{n-1}}{2} - \frac{\hat{k}_{x}u_{n+1}}{2} = -\operatorname{Re}^{-1}|\hat{k}_{n}|^{2}u_{n} - \operatorname{Ro}^{-1}w_{n},$$

$$+ \frac{\hat{k}_{x}}{\hat{k}_{y}} \left[\hat{\lambda}v_{n} + \frac{\hat{k}_{x}v_{n-1}}{2} - \frac{\hat{k}_{x}v_{n+1}}{2} + \operatorname{Re}^{-1}|\hat{k}_{n}|^{2}v_{n} \right]$$

$$\hat{\lambda}w_{n} + \frac{\hat{k}_{x}w_{n-1}}{2} - \frac{\hat{k}_{x}w_{n+1}}{2} = \operatorname{Ri}T_{n} - \operatorname{Re}^{-1}|\hat{k}_{n}|^{2}w_{n} + \operatorname{Ro}^{-1}u_{n}$$

$$+ \frac{\hat{k}_{z}}{\hat{k}_{y}} \left[\hat{\lambda}v_{n} + \frac{\hat{k}_{x}v_{n-1}}{2} - \frac{\hat{k}_{x}v_{n+1}}{2} + \operatorname{Re}^{-1}|\hat{k}_{n}|^{2}v_{n} \right]$$

$$\hat{\lambda}T_{n} + \frac{\hat{k}_{x}T_{n-1}}{2} - \frac{\hat{k}_{x}T_{n+1}}{2} + w_{n} = -\operatorname{Pe}^{-1}|\hat{k}_{n}|^{2}T_{n}$$

$$\hat{k}_{x}u_{n} + \hat{k}_{y}v_{n} + nw_{n} = 0.$$
(19)

This now takes the form of a generalized eigenvalue problem, namely

$$\mathbf{A}(\text{Re, Ri, Pe, Ro, } \hat{k}_x, \hat{k}_y)X = \hat{\lambda}\mathbf{B}X, \tag{20}$$

where $X = (u_{-N}, \dots, u_N, v_{-N}, \dots, v_N, w_{-N}, \dots, w_N, T_{-N}, \dots, T_N)$ is the solution vector for some finite N, and \mathbf{A} and \mathbf{B} are two $4(2N+1) \times 4(2N+1)$ matrices. This problem can be solved numerically for $\hat{\lambda}$ for any given set of parameters (Re, Pe, Ri, Ro), and selected horizontal wavenumbers \hat{k}_x and \hat{k}_y . Note that there are, by construction, 4(2N+1) possible eigenvalues and eigenvectors of this system. However, we only keep the solution for which the real part of $\hat{\lambda}$ is largest, and call it $\hat{\lambda}(\text{Re}, \text{Pe}, \text{Ri}, \text{Ro}, \hat{k}_x, \hat{k}_y)$.

3.2 Two remarkable limits

Although we generally need to solve the system numerically, two remarkable limits can be derived analytically from the system of equations (15). The first limit is obtained assuming invariance of the perturbations in the y-direction, so $\partial/\partial \hat{y} = 0$. The incompressibility condition then reduces to

$$\frac{\partial \hat{u}'}{\partial \hat{x}} + \frac{\partial \hat{w}'}{\partial \hat{z}} = 0. \tag{21}$$

By taking the \hat{z} -derivative of the *x*-momentum equation and the \hat{x} -derivative of the *z*-momentum equation, one arrives at the following two equations:

$$\begin{split} \frac{\partial}{\partial \hat{z}} \left(\frac{\partial \hat{u}'}{\partial \hat{t}} + \hat{w}' \frac{\mathrm{d}\hat{u}_L}{\mathrm{d}\hat{z}} + \hat{u}_L \frac{\partial \hat{u}'}{\partial \hat{x}} \right) &= \frac{\partial}{\partial \hat{z}} \left(-\frac{\partial \hat{p}'}{\partial \hat{x}} + \frac{1}{\mathrm{Re}} \nabla^2 \hat{u}' \right) - \frac{1}{\mathrm{Ro}} \frac{\partial \hat{w}'}{\partial \hat{z}}, \\ \frac{\partial}{\partial \hat{x}} \left(\frac{\partial \hat{w}'}{\partial \hat{t}} + \hat{u}_L \frac{\partial \hat{w}'}{\partial \hat{x}} \right) &= \frac{\partial}{\partial \hat{x}} \left(-\frac{\partial \hat{p}'}{\partial \hat{z}} + \mathrm{Ri}\hat{T}' + \frac{1}{\mathrm{Re}} \nabla^2 \hat{w}' \right) + \frac{1}{\mathrm{Ro}} \frac{\partial \hat{u}'}{\partial \hat{x}}, \end{split}$$
(22)

which are the only remaining equations directly affected by rotation. If we subtract one from the other, and use the incompressibility condition (21), terms containing Ro disappear from the system to yield.

$$\begin{split} &\frac{\partial}{\partial \hat{t}} \left(\frac{\partial \hat{u}'}{\partial \hat{z}} - \frac{\partial \hat{w}'}{\partial \hat{x}} \right) + \left(\frac{\partial}{\partial \hat{z}} \left(\hat{u}_L \frac{\partial \hat{u}'}{\partial \hat{x}} \right) - \hat{u}_L \frac{\partial^2 \hat{w}'}{\partial \hat{x}^2} \right) + \frac{\partial}{\partial \hat{z}} \left(\hat{w}' \frac{d\hat{u}_L}{d\hat{z}} \right) \\ &= - \text{Ri} \frac{\partial \hat{T}'}{\partial \hat{x}} + \frac{1}{\text{Re}} \nabla^2 \left(\frac{\partial \hat{u}'}{\partial \hat{z}} - \frac{\partial \hat{w}'}{\partial \hat{x}} \right). \end{split} \tag{23}$$

This shows that rotation has no effect on the linear evolution of \hat{y} -invariant perturbations in the equatorial regions of a star. Hence, we expect to recover the stability properties of standard diffusive stratified shear instabilities for $\hat{k}_y = 0$ modes, regardless of the rotation rate (see e.g. Garaud et al. 2015).

On the other hand, if we assume x-invariance $(\partial/\partial \hat{x} = 0)$, (15) reduces to the following set of PDEs:

$$\begin{split} \frac{\partial \hat{u}'}{\partial \hat{t}} + \hat{w}' \frac{d\hat{u}_L}{d\hat{z}} &= \frac{1}{\text{Re}} \nabla^2 \hat{u}' - \frac{\hat{w}'}{\text{Ro}}, \\ \frac{\partial \hat{v}'}{\partial \hat{t}} &= -\frac{\partial \hat{p}'}{\partial \hat{y}} + \frac{1}{\text{Re}} \nabla^2 \hat{v}', \\ \frac{\partial \hat{w}'}{\partial \hat{t}} &= -\frac{\partial \hat{p}'}{\partial \hat{z}} + \text{Ri}\hat{T}' + \frac{1}{\text{Re}} \nabla^2 \hat{w}' + \frac{\hat{u}'}{\text{Ro}}, \\ \frac{\partial \hat{T}'}{\partial \hat{t}} + \hat{w}' &= \frac{1}{\text{Pe}} \nabla^2 \hat{T}', \\ \frac{\partial \hat{v}'}{\partial \hat{y}} + \frac{\partial \hat{w}'}{\partial \hat{z}} &= 0. \end{split}$$

$$(24)$$

If, for the moment, we further assume that the vertical scale of the instability is much smaller than the characteristic length-scale of the shear (which can be verified a posteriori), then we can approximate the shear to be locally constant¹ with a value \hat{S} . The system now has constant coefficients, and we can successively eliminate variables to arrive at the following equation:

$$\hat{D}_{u}^{2}\hat{D}_{T}\nabla^{2}\hat{w}' = -\left[\frac{1}{\text{Ro}}\hat{D}_{T}\left(\frac{1}{\text{Ro}} + \hat{S}\right) + \text{Ri}\hat{D}_{u}\right]\frac{\partial^{2}\hat{w}'}{\partial\hat{y}^{2}},\tag{25}$$

where \hat{D} 's are shorthand notations for the differential operators:

$$\hat{D}_{u} = \frac{1}{\text{Re}} \nabla^{2} - \frac{\partial}{\partial \hat{t}}, \quad \hat{D}_{T} = \frac{1}{\text{Pe}} \nabla^{2} - \frac{\partial}{\partial \hat{t}}.$$
 (26)

We assume normal mode solutions of the form $\hat{w}' \propto \exp(i\hat{k}_y\hat{y} + i\hat{k}_z\hat{z} + \hat{\lambda}\hat{t})$ and obtain the algebraic equation:

$$\left(\frac{\hat{K}^2}{\text{Re}} + \hat{\lambda}\right)^2 \left(\frac{\hat{K}^2}{\text{Pe}} + \hat{\lambda}\right) = -\left(\frac{\hat{K}^2}{\text{Pe}} + \hat{\lambda}\right) \left[\frac{1}{\text{Ro}} \left(\frac{1}{\text{Ro}} + \hat{S}\right) + \text{Ri} \left(\frac{\hat{K}^2}{\text{Re}} + \lambda\right)\right] \frac{\hat{k}_y^2}{\hat{K}^2}, \tag{27}$$

¹A more formal approach would involve using a JWKB approximation on the governing equations.

where $\hat{K}^2 = \hat{k}_y^2 + \hat{k}_z^2$. This can be expanded to give a third-order polynomial equation in $\hat{\lambda}$:

$$\hat{\lambda}^{3} + a_{2}\hat{\lambda}^{2} + a_{1}\hat{\lambda} + a_{0} = 0,$$

$$a_{2} = \left(\frac{1}{Pe} + \frac{2}{Re}\right)\hat{K}^{2},$$

$$a_{1} = \left(\frac{2}{RePe} + \frac{1}{Re^{2}}\right)\hat{K}^{4} + Ri\frac{\hat{k}_{y}^{2}}{\hat{K}^{2}} + \frac{1}{Ro}\left(\frac{1}{Ro} + \hat{S}\right)\frac{\hat{k}_{y}^{2}}{\hat{K}^{2}},$$

$$a_{0} = \frac{\hat{K}^{6}}{Re^{2}Pe} + Ri\frac{\hat{k}_{y}^{2}}{Re} + \frac{\hat{k}_{y}^{2}}{RoRe}\left(\frac{1}{Ro} + \hat{S}\right).$$
(28)

The absence of any solution with positive real part (which is necessary for stability) can be established using the Routh–Hurwitz theorem. For a third-order polynomial, the Routh–Hurwitz criterion for stability is satisfied if and only if a_2 , $a_0 > 0$ and $a_2a_1 > a_0$ (Anagnost & Desoer 1991). Specifically, the condition $a_0 > 0$ gives the following inequality:

$$\frac{1}{\mathrm{Re}^2} \frac{\hat{K}^6}{\hat{k}_z^2} > -\frac{1}{\mathrm{Ro}} \left(\frac{1}{\mathrm{Ro}} + \hat{S} \right) - \mathrm{RiPr}. \tag{29}$$

For this to be true for any value of \hat{k}_y , $\hat{k}_z \neq 0$, the RHS must be non-positive. In other words, the system is stable to all possible modes provided $0 \geq -\text{Ro}^{-1} \left(\text{Ro}^{-1} + \hat{S} \right) - \text{RiPr}$ and conversely, can be unstable to some modes provided

$$0 > \frac{1}{\text{Ro}} \left(\frac{1}{\text{Ro}} + \hat{S} \right) + \text{RiPr.}$$
 (30)

This is the non-dimensional equivalent of the GSF instability criterion (5).

This detour has enabled us to identify analytically two distinct modes of instability: the first one is a pure shearing mode, with $\hat{k}_y = 0$, that does not know about rotation; the second one has $\hat{k}_x = 0$, and is a standard 2D GSF mode (see above). As we shall see below, one or the other of these two modes tends to dominate the linear stability of the system in almost all of the parameter space.

4 LINEAR STABILITY RESULTS

In this section, we now present and discuss the results of the linear stability analysis outlined in Section 3. In what follows, we compute the fastest-growing perturbations to the stratified, rotating shear flow $u_L(\hat{z})$, for a given set of model parameters (Re, Pe, Ri, Ro), by maximizing $\Re[\hat{\lambda}(\text{Re}, \text{Pe}, \text{Ri}, \text{Ro}, \hat{k}_x, \hat{k}_y)]$ over all possible values of the horizontal wavenumbers \hat{k}_x and \hat{k}_y . The maximization problem then returns the growth rate and wavenumbers of the fastest-growing modes. The latter are presented, for fixed Re = 10 000 and varying Pe, Ri, and Ro, in Fig. 2.

Each row of Fig. 2 corresponds to a particular value of Pe, ranging from 1000 (top row, weak thermal diffusion) down to 0.1 (bottom row, strong thermal diffusion). In each row, the left-side panel shows the real part of the growth rate (denoted for simplicity with $\hat{\lambda}$), the middle panel shows the wavenumber \hat{k}_x , and the right-side panel shows the wavenumber \hat{k}_y , of the fastest-growing modes. Finally, within each panel, the quantity in question is shown as a colour map, as a function of the Richardson number Ri (horizontal axis) and the inverse Rossby number Ro⁻¹ (vertical axis). Stratification increases as Ri increases, and the rotation rate increases as Ro⁻¹ increases (see equation 14). If the system is linearly stable, the quantity is rendered using the white colour.

Overall, we clearly see the emergence of (at least) two distinct modes of instability, whose relative importance (in terms of which

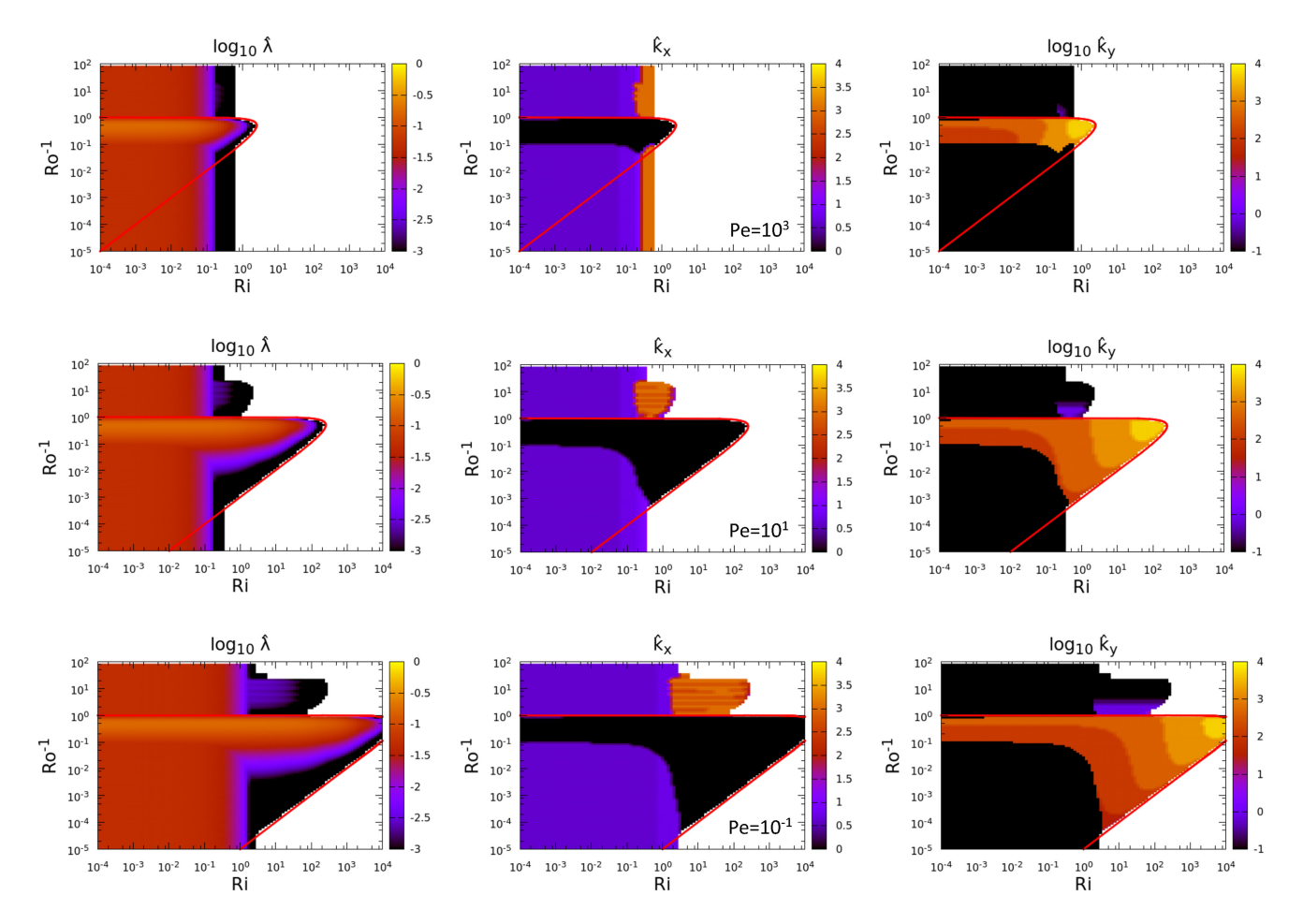


Figure 2. Linear stability analysis results. From left to right: growth rate map (log colour bar), x-wavenumber map (linear colour bar), and y-wavenumber map (log colour bar). White areas are regions that are linearly stable. The red line is the marginal stability boundary for the GSF instability. Re = 10 000 for all maps. From top to bottom: Pe = 1000, 10, 0.1.

has the largest growth rate) depends on the input parameters. The first mode has $\hat{k}_v = 0$, $\hat{k}_x = O(1)$, and a growth rate $\hat{\lambda}$ that appears to be independent of the rotation rate. The mode is stabilized if Ri exceeds a certain threshold. The second mode has $\hat{k}_x = 0$, a \hat{k}_y that can be significantly greater than one, and dominates in a region of the (Ri, Ro⁻¹) plane whose shape is somewhat reminiscent of a plough. Based on the analysis of Section 3.2, we see that the first mode is clearly a shearing mode, while the second is clearly a GSF mode. This is also confirmed by plotting the marginal stability curve associated with the GSF instability in red (see equation 30); the region below and to the left of the red curve is linearly unstable to GSF perturbations. We therefore conclude that there is a substantial range of parameters for which the GSF instability and the shear instability can in principle coexist, even if one dominates over the other from a linear perspective. Finally, we also note that there appears to be a third, fully 3D mode present for large rotation rate and intermediate stratification, that we will not discuss in this paper (as its physical interpretation is not well understood).

In the weakly rotating limit, $(Ro^{-1} \rightarrow 0)$, the GSF mode is either stabilized or subdominant, and the shearing mode dominates. The growth rate of the shear instability tends to a constant of the order of 0.1 in the limit of weak stratification, and drops to zero as Ri exceeds a certain threshold whose value depends on the Péclet number. We can see from Fig. 2 that the neutral stability line lies close to one at large Péclet number. This may seem surprising at first given that

the Richardson criterion states that stratified shear flows are linearly stable if the gradient Richardson number, which is equal to $J = \mathrm{Ri}/\cos^2(\hat{z})$ in this problem, is greater than 1/4 everywhere in the flow, which happens as soon as Ri > 1/4. This apparent discrepancy can be resolved by noting that the standard Richardson criterion neglects viscous effects, and thus fails to capture viscous instabilities. Between Ri = 1/4 and Ri = 1, viscous modes exist and can be distinguished by their small growth rates. This has been shown by Balmforth & Young (2002) in the case of stratified 2D sinusoidal shear flows and by Garaud et al. (2015) in the case of stratified 3D sinusoidal shear flows.

As Pe decreases below unity, the critical value of the Richardson number for shear instability Ri_c increases, consistent with the results of Garaud et al. (2015), who demonstrated that the marginal stability criterion satisfies $\mathrm{Ri}_c = O(\mathrm{Pe}^{-1})$ for a low Péclet number sinusoidal flow. Since the inverse of the Péclet number represents how thermally diffusive the system is, decreasing Pe is equivalent to increasing thermal diffusion in the system. Faster thermal diffusion acts as a destabilizing agent against the density stratification, allowing for the existence of unstable modes at higher values of Ri.

Finally, it is worth remembering that the shear instability has a subcritical (non-linear) branch (see Section 1). This subcritical instability does not appear in this linear stability figure, but can be excited by finite-amplitude perturbations of the right shape provided the product of the local Richardson number and the Prandtl number

is lower than approximately 0.007 (at least in the non-rotating case, see Zahn 1974; Prat et al. 2016; Garaud et al. 2017). Since Pr=0.1 in the top row, 0.001 in the middle row, and 0.00001 in the bottom row, this non-linear branch is irrelevant in the top row, but would exist up to $Ri \simeq 7$ and $Ri \simeq 700$ in the middle and bottom rows, respectively.

At higher rotation rates (larger Ro⁻¹), the GSF mode emerges, and dominates in the plough-shaped region described earlier. For large Pe (top row), this region has a fairly limited extent, but expands as Pe decreases (middle and bottom rows) to encompass higher values of the stratification and lower rotation rates, consistent with the criterion in equation (30), red line. Within the GSF region, we see that the *y*-wavenumber of the fastest growing GSF mode tends to increase as Ri increases. This can be understood noting that GSF instabilities are analogous to double diffusive fingering instabilities, whose characteristic wavenumber is proportional to Ra^{1/4} in the non-dimensionalization used here, where Ra = PeReRi is the Rayleigh number. At constant Re and Pe, an increase in Ri therefore implies an increase in the characteristic wavenumber of the fastest growing mode.

In summary, we see that this model system has the potential for a wide range of interesting dynamics, raising many questions that are of relevance to mixing in stars, and of theoretical interest in fluid dynamics. In particular, it will be interesting to determine (1) which linear mode of instability ends up dominating the system dynamics in the regions of parameter space where both coexist, and (2) what happens when the GSF coexists with the subcritical branch of the shear instability.

5 NUMERICAL SIMULATIONS

In what follows, we now turn to DNS to study the non-linear aspects of instabilities of rotating diffusive stratified shear flows. We begin by briefly describing the algorithm and model set-up used in the numerical experiments, before presenting the evolution of a characteristic simulation.

5.1 Numerical code: PADDI

The numerical experiments presented in this work were performed using the PADDI code. PADDI is a high-performance pseudo-spectral code originally developed to solve double-diffusive hydrodynamic equations over a triply periodic 3D domain (Stellmach et al. 2011). Salient aspects of the code are presented in Traxler, Garaud & Stellmach (2011). The original code was modified to include both the Coriolis force (Moll & Garaud 2017) and a sinusoidal body force (Garaud et al. 2015) to suit the needs of the study.

5.2 Forcing-based non-dimensionalization

For the purpose of the linear stability analysis presented in Sections 3 and 4, we employed a non-dimensionalization based on the amplitude of the laminar steady-state solution, $U_L = F_0/(\rho_{\rm m} v k_s^2)$. This non-dimensionalization is useful when looking at the early stages of development of the instability starting from the laminar solution, but is not appropriate once the flow becomes non-linear, and the mean shear decreases as a result of momentum transport by the turbulence. Garaud & Kulenthirarajah (2016) proposed that a more relevant non-dimensionalization in turbulent, non-rotating, shear flows can be derived from assuming a balance between inertial terms and the

forcing in the momentum equation, such that:

$$\rho_{\mathbf{m}}(\boldsymbol{u}\cdot\nabla\boldsymbol{u})\cdot\hat{\boldsymbol{e}}_{x}\sim F_{0}.\tag{31}$$

Then, we can define a new flow amplitude U_F as:

$$U_F = \left(\frac{F_0}{k_s \rho_m}\right)^{1/2}.\tag{32}$$

This velocity scale is independent of any diffusivity, and thus ought to be more relevant than U_L once turbulence has fully developed.

Interestingly, the quantities U_F and U_L , respectively, can now be seen as estimates for the minimum and maximum possible amplitudes of the body-forced mean flow achievable in a statistically stationary state for the selected model set-up. Indeed, the amplitude of the mean flow is expected to be largest in the absence of any turbulent dissipation, where it takes the value U_L , while it is expected to be smallest when the turbulent viscosity is largest. Hidden in the dimensional argument above is the assumption that the turbulent eddies have (1) a length-scale of order k_s^{-1} and (2) a characteristic velocity of the order of the mean flow velocity. These are the largest possible length- and velocity scales for this flow, so the corresponding turbulent viscosity implied in this argument is also the largest one achievable. Hence U_F is an estimate of the smallest mean flow amplitude achievable in this set-up.

Using a new system of units where the velocities are scaled by U_F instead of U_L (and the unit time-scale is correspondingly changed to $1/k_sU_F$), we obtain a set of non-dimensional equations that looks almost identical to the system (13):

$$\frac{\mathbf{D}\check{\boldsymbol{u}}}{\mathbf{D}\check{\boldsymbol{t}}} = -\nabla\check{\boldsymbol{p}} + \mathbf{R}\mathbf{i}_{F}\check{\boldsymbol{T}}\hat{\boldsymbol{e}}_{z} + \frac{1}{\mathbf{R}\mathbf{e}_{F}}\nabla^{2}\check{\boldsymbol{u}} - \frac{\check{\boldsymbol{w}}}{\mathbf{R}\mathbf{o}_{F}}\hat{\boldsymbol{e}}_{x} + \frac{\check{\boldsymbol{u}}}{\mathbf{R}\mathbf{o}_{F}}\hat{\boldsymbol{e}}_{z} + \sin\check{\boldsymbol{z}}\hat{\boldsymbol{e}}_{x},
\frac{\partial\check{\boldsymbol{T}}}{\partial\check{\boldsymbol{t}}} + \check{\boldsymbol{u}} \cdot \nabla\check{\boldsymbol{T}} + \check{\boldsymbol{w}} = \frac{1}{\mathbf{P}\mathbf{e}_{F}}\nabla^{2}\check{\boldsymbol{T}},
\nabla \cdot \check{\boldsymbol{u}} = 0,$$
(33)

where $\check{\boldsymbol{u}} = \boldsymbol{u}/U_F$, $\check{t} = tU_F k_s$, $\check{T} = \hat{T}$, and where

$$Re_{F} = \frac{U_{F}}{k_{s}\nu} = \left(\frac{F_{0}}{\rho_{m}\nu^{2}k_{s}^{3}}\right)^{1/2} = Re^{1/2},$$

$$Ri_{F} = \frac{N^{2}}{U_{F}^{2}k_{s}^{2}} = \frac{N^{2}\rho_{m}}{k_{s}F_{0}} = ReRi,$$

$$Pe_{F} = \frac{U_{F}}{k_{s}\kappa_{T}} = \left(\frac{F_{0}}{\rho_{m}\nu k_{s}^{3}\kappa_{T}^{2}}\right)^{1/2} = Re^{-1/2}Pe,$$

$$Ro_{F} = \frac{k_{s}U_{F}}{2\Omega_{0}} = \left(\frac{k_{s}F_{0}}{4\Omega_{0}^{2}\rho_{m}}\right)^{1/2} = Re^{-1/2}Ro.$$
(34)

The numerical results described in the following sections will be given in this new non-dimensionalization. Note that since the unit length-scale has not changed, $\hat{x} = \check{x}$, and similarly for \check{y} and \check{z} . Garaud & Kulenthirarajah (2016) demonstrated that Re_F , Pe_F , and Ri_F are relatively good estimates for the actual turbulent Reynolds, Péclet, and Richardson numbers in *non-rotating* stratified shear flows driven by a body force. This is not necessarily true anymore in the rotating case, but this system of units is still more appropriate than the one based on the laminar flow.

5.3 Characteristic simulation output

We begin by presenting the evolution of a characteristic simulation, whose governing parameters are $Re_F = 100$, $Pe_F = 0.1$, $Ri_F = 1000$, and $Ro_F^{-1} = 1$, or equivalently in the non-dimensionalization based on the laminar flow, $Re = 10\,000$, Pe = 10, Ri = 0.1, and $Ro^{-1} = 0.01$. According to the linear stability analysis of the previous section,

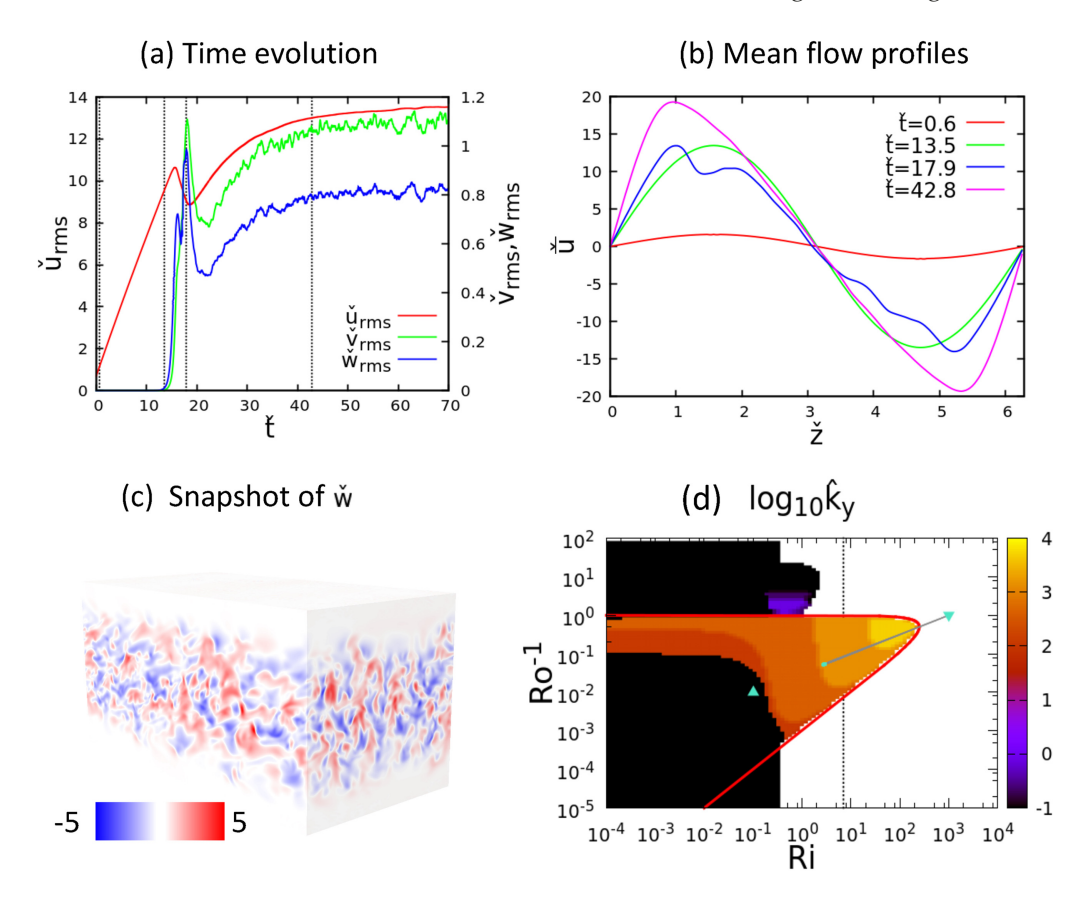


Figure 3. Characteristic simulation with governing parameters $Re_F = 100$, $Pe_F = 0.1$, $Ri_F = 1000$, and $Ro_F^{-1} = 1$, or equivalently in the non-dimensionalization based on the laminar flow, $Re = 10\,000$, Pe = 10, Ri = 0.1, and $Ro^{-1} = 0.01$. Panel (a): time evolution of \check{u}_{rms} , \check{v}_{rms} , and \check{w}_{rms} . Panel (b): snapshots of the z-profiles of the mean flow \check{u} . The times correspond to the dotted grey lines in (a). Panel (c): a representative snapshot of \check{w} taken at $\check{t} = 42.5$. The axes are such that x is along the long direction of the domain, and z points upwards. Panel (d): the trajectory of the simulation (thin grey line) and steady state (thick cyan line) plotted over the linear stability map in $\log_{10} \hat{k}_y$. It lies between two triangles which denote the laminar limit (upwards triangle) and the fully turbulent limit (inverted triangle). The simulation is initialized in the linearly stable region and ends up in a statistically steady state in the GSF-dominated region. The dashed solid line shows the extent of the subcritical branch of diffusive shear instability (assuming it is not affected by rotation).

the fastest-growing mode of instability starting from the laminar equilibrium state should be a shearing mode. The non-dimensional numerical domain size is ($\check{L}_x = 4\pi$, $\check{L}_y = 2\pi$, $\check{L}_z = 2\pi$), which is sufficiently long to allow for the natural development of the basic shear instability without constraining the flow too much. Since the GSF modes are smaller scale, this domain size ought to be sufficient in the GSF limit as well. The numerical resolution selected for this simulation has $384 \times 192 \times 192$ equivalent grid points.

The simulation is initialized with a sinusoidal streamwise flow profile given by $\check{u}_0(\check{x},\check{y},\check{z},0)=\sin(\check{z})$, plus small random perturbations that seed the instabilities. We note that this flow is *not* the laminar equilibrium solution for the system (which would have an amplitude of Re_F in this non-dimensionalization). Instead, the flow is stable at time $\check{t}=0$. The evolution of various quantities of interest with time is presented in Fig. 3.

Fig. 3(a) shows the evolution of $\check{u}_{rms}(\check{t})$, $\check{v}_{rms}(\check{t})$, and $\check{w}_{rms}(\check{t})$, where

$$\check{u}_{\text{rms}}(\check{t}) = \left(\frac{1}{\check{L}_x \check{L}_y \check{L}_z} \int_D \check{u}^2(\check{x}, \check{t}) d^3 \check{x}\right)^{1/2},$$
(35)

(and similarly for \check{v} and \check{w}). The constant forcing in the streamwise direction causes the amplitude of the sinusoidal flow [and therefore $\check{u}_{rms}(\check{t})$] to increase linearly with time until about $\check{t}=15$, where it reaches the linear instability threshold for GSF modes to grow. At this point, perturbations begin to grow exponentially [see e.g. $\check{v}_{rms}(\check{t})$

and $\check{w}_{rms}(\check{t})$]. Visual inspection of \check{w} shows that the perturbations are limited spatially to the region where the mean shear is negative, and are initially invariant in \check{x} , which is as expected from the GSF instability. Eventually, the perturbations begin to affect the mean flow and non-linear saturation occurs around $\check{t}=20$. At this point, the turbulence is still limited to regions of negative shear, but has become fully 3D, as illustrated in the snapshot of \check{w} taken at $\check{t}=43$ (see Fig. 3c). The shear in the laminar regions continues to grow slowly on a viscous time-scale in response to the imposed forcing, until the system finally reaches a statistically stationary state around $\check{t}=70$.

Fig. 3(b) shows the mean streamwise flow profile

$$\check{u}(\check{z},\check{t}) = \frac{1}{\check{L}_x \check{L}_y} \int_0^{\check{L}_x} \int_0^{\check{L}_y} \check{u}(\check{x},\check{y},\check{z},\check{t}) d\check{x} d\check{y} \tag{36}$$

at selected times. It has a perfect sinusoidal shape at early times, but acquires a marked asymmetry once the GSF instability develops, whereby the turbulent region for $1 < \check{z} < 5$ has a weaker shear, while the laminar regions for $0 < \check{z} < 1$ and $5 < \check{z} < 2\pi$ have a much larger shear. To understand why the mean flow becomes strongly asymmetric, note that the horizontal average of the momentum equation is

$$\frac{\partial \check{u}}{\partial \check{t}} + \frac{\partial}{\partial \check{z}} (\overline{\check{u}}\overline{\check{w}}) = \frac{1}{\text{Re}_E} \frac{\partial^2 \check{u}}{\partial \check{z}^2} + \sin(\check{z}), \tag{37}$$

where $\check{u}\check{w}$ is the Reynolds stress. Assuming that this turbulent stress behaves in a diffusive manner, we can define a turbulent diffusivity \check{v}_{turb} in the usual way,

$$\overline{\check{u}\check{w}} = -\check{v}_{\text{turb}}\frac{\partial \check{u}}{\partial \check{z}},\tag{38}$$

in which case (37) becomes

$$\frac{\partial \check{u}}{\partial \check{t}} = \frac{\partial}{\partial \check{z}} \left[(Re_F^{-1} + \check{v}_{turb}) \frac{\partial \check{u}}{\partial \check{z}} \right] + \sin(\check{z}). \tag{39}$$

In a statistically stationary state, the time derivative can be ignored, and integration in \check{z} yields:

$$\frac{\partial \check{u}}{\partial \check{z}} = \frac{\cos(\check{z})}{\operatorname{Re}_F^{-1} + \check{\nu}_{\text{turb}}}.$$
(40)

This shows that the amplitude of the mean shear $\partial \check{u}/\partial \check{z}$ must be weaker in turbulent regions (assuming $\check{v}_{turb} > 0$), and stronger in laminar regions where $\hat{v}_{turb} \simeq 0$).

To understand why the system ends up being governed by the GSF instability rather than the shear instability, we compute the 'trajectory' of the simulation on the (Ri, Ro⁻¹) stability diagram. To do so, note that if we allow ourselves to approximate the mean flow profile by the formula $\check{u}(\check{z},\check{t})\simeq \check{A}(\check{t})\sin(\check{z})$, with $\check{A}(\check{t})$ varying slowly with time, then we can use the frozen-in approximation to perform a linear stability of this flow at any time \check{t} . This is easily done by solving the linear system (19), with (Re, Pe, Ri, Ro) replaced by effective parameters (Re_{eff}, Pe_{eff}, Ri_{eff}, Ro_{eff}), where

$$Re_{eff} = \frac{\check{A}U_F}{\nu k_e} = \check{A}Re_F \tag{41}$$

$$Pe_{eff} = \frac{\check{A}U_F}{\kappa_T k_s} = \check{A}Pe_F \tag{42}$$

$$Ri_{eff} = \frac{N^2}{\check{A}^2 U_r^2 k^2} = \frac{Ri_F}{\check{A}^2}$$
(43)

$$Ro_{\text{eff}} = \frac{k_s \check{A} U_F}{2\Omega_0} = \check{A} Ro_F. \tag{44}$$

We can verify that this is indeed consistent: the laminar steady-state solution has amplitude $\check{A}=\mathrm{Re}_F$, and in that case $\mathrm{Re}_\mathrm{eff}=\mathrm{Re}_F^2=\mathrm{Re}$ (and similarly for the other parameters), so we indeed recover (19). With $\check{A}=1$, by contrast, $\mathrm{Re}_\mathrm{eff}=\mathrm{Re}_F$ (and similarly for the other parameters), which gives an estimate of the stability of the system in its 'weakest shear' configuration. In practice, we obtain a quick estimate of $\check{A}(\check{t})$ using $\check{A}(\check{t})\simeq\sqrt{2}\check{u}_\mathrm{rms}(\check{t})$; this approximation would be exact if the mean flow were exactly sinusoidal (which is not the case in the GSF-dominated simulations) and if the perturbations were much smaller than the mean (which is not the case in the weakly stratified simulations). We checked that turbulent mixing does not affect the stratification significantly in the statistically stationary state of each simulation, so N^2 remains roughly constant in time and space.

With these simplifications and caveats in mind, the trajectory of the fiducial simulation on the (Ri, Ro⁻¹) diagram is shown in Fig. 3(d). We see that it starts at $\check{t}=0$ on the top right inverted triangle when $\check{A}=1$, which is in the linearly stable region, then moves towards the bottom left on a straight line. Note that because the only varying quantity in this expression is $\check{A}(t)$, simulation trajectories satisfy $\mathrm{Ro}_{\mathrm{eff}}^{-1} \propto \mathrm{Ri}_{\mathrm{eff}}^{1/2}$ at all times, and therefore appear as straight lines in the (Ri, Ro⁻¹) stability diagram (which uses logarithmic axes). When the line intersects the GSF-unstable region the flow becomes unstable, and then continues to move downward and to the left as the mean flow continues to increase slowly in amplitude (see above). The trajectory stops before it reaches the shear-unstable region (where the laminar

steady-state solution resides, and is marked by an upright triangle). As a result, and consistent with the findings above, the statistically stationary state is one that is dominated by the GSF instability. We note that the system could also be non-linearly unstable to the diffusive shear instability at these parameters. However, visual inspection of the simulation shows that this does not appear to be the case (see also Section 6).

It is important to keep in mind that this visualization of the simulation trajectory should only be used for qualitative purposes. Indeed, the background image of $\log_{10} \check{k}_y$ on which the trajectory is superimposed was produced using a fixed Reynolds number Re = 10 000 and a fixed Péclet number Pe = 10, whereas in practice both Re_{eff} and Pe_{eff} evolve with time with \check{A} . A more useful visualization can be created in the 3D parameter space of (Ri, Ro⁻¹, Re) (noting that Pe_{eff} = Pr Re_{eff} where the Prandtl number is constant), but this is difficult to show in a printed figure.

In what follows, we now analyse a number of simulations with widely varying parameters, and attempt to characterize the dynamics observed based on the tools and arguments presented in this section.

5.4 Exploration of parameter space

We fix $Re_F = 100$ and $Pe_F = 0.1$ (so Pe = 0.001), and vary both Ri_F and Ro_F^{-1} to explore parameter space. Table 1 lists the input parameters and summarizes salient results for all available simulations. In all cases, the non-dimensional domain size is $(4\pi, 2\pi, 2\pi)$. Each simulation has a numerical resolution of $384 \times 192 \times 192$ equivalent grid points and is either initialized from small random perturbations to a laminar solution, or from the endpoint of another simulation ran at slightly different input parameters.

To illustrate the wide range of possible emergent dynamics, we consider a subset of the data for three possible values of the input Richardson number ($Ri_F = 1, 100, 10000$), and three possible values of the input inverse Rossby number ($Ro_F^{-1} = 0.2, 1, 5$). Fig. 4 (top row) shows where these simulations lie in parameter space as follows. Each simulation is assigned a colour. The full possible extent of its trajectory in parameter space is shown as a thin grey segment of slope 1/2 (see the discussion of Fig. 3d), ranging between the laminar state ($\check{A} = \operatorname{Re}_F$, upright triangle) and the most turbulent state ($\mathring{A} = 1$, inverted triangle). For each simulation, we waited until the system reached a statistically stationary state, then plotted the range of the trajectory in that state. With that choice, the simulation appears as a coloured point if fluctuations in $\check{A}(\check{t})$ are small, and as a coloured segment if fluctuations in $\check{A}(\check{t})$ are large. The left column of Fig. 4 shows this information on a background colour map of $\log_{10} \hat{k}_{y}$ obtained from a linear stability analysis using $Re_{eff} = Re = 10000$, $Pe_{eff} = Pe = 10$, while the right column shows the same information superimposed on a similar colour map obtained using $Re_{eff} = Re_F =$ 100, $Pe_{eff} = Pe_F = 0.1$. Comparing the two maps provides an idea of whether one can reliably identify a mode as being 'shear-dominated' or 'GSF-dominated' using linear stability analysis alone, showing that in some of the more clear-cut cases we can, but that in general we cannot (see more on this below).

Figs 5 and 6 show representative snapshots of \check{u} and \check{w} , respectively, in the same simulations, once they have achieved a statistically stationary state. The snapshots are arranged in the same way as the triangles in the top row of Fig. 4: each row from bottom to top corresponding to an increasing value of the rotation rate $(Ro_F^{-1} = 0.2, 1, 5)$, and each column from left to right corresponding to an increasing value of the stratification $(Ri_F = 1, 100, 10\,000)$.

We begin by looking at the most weakly rotating simulations (bottom row of Figs 5 and 6). In the left-hand and centre panels, the

Table 1. Salient properties of all available simulations. Columns 1 and 2 list the governing parameters Re_F^{-1} and Re_F^{-1} and Re

Ro_F^{-1}	Ri_F	$\check{u}_{ m rms}$	$\check{w}_{ m rms}$	$\check{S}_{ m mid}$	$\check{ u}_{turb}$
0.2	1	1.8(2)	1.19(9)	- 1.7(4)	0.7(2)
0.2	10	2.8(1)	1(5)	-2.7(6)	0.5(1)
0.2	100	4.92(7)	0.89(3)	-5.4(6)	0.2(3)
0.2	1000	16.1(2)	0.79(2)	-13.5(8)	0.1(1)
$0.2^{(a)}$	4000	34.4(4)	0.061(2)	-37(7)	0.014(5)
$0.2^{(b)}$	4000	28.9(4)	0.8(1)	-25(1)	0.07(2)
0.2	10 000	57.3(7)	0.033(2)	-68(6)	0.006(2)
1	1	1.9(1)	1.4(1)	-1.6(4)	0.7(3)
1	10	2.3(3)	1.12(9)	-1.9(6)	0.8(3)
1	100	4.9(2)	0.96(6)	-4.3(6)	0.34(7)
1	1000	13.55(8)	0.82(2)	-11.4(8)	0.13(1)
1	10 000	34.5(2)	0.43(4)	-33(1)	0.03(4)
5	1	2(4)	2(4)	-1.8(6)	0.5(5)
5	10	4.1(9)	1.5(4)	-4(1)	0(3)
5	100	7.6(1)	1.35(7)	-6(4)	0.26(4)
5	1000	11.29(4)	0.95(2)	-9(7)	0.17(2)
5	10 000	23.3(2)	0.59(1)	-20.9(9)	0.059(5)
5	100 000	44.6(9)	0.12(1)	-50(5)	0.012(2)

- (a) data extracted in the time interval $(\check{t} \check{t}_{ref}) \in [31.2, 38.2]$ (see Fig. 11).
- (b) data extracted in the time interval $(\check{t} \check{t}_{ref}) \in [44.2, 51.2]$ (see Fig. 11).

effect of rotation appears at a first glance to be negligible and the snapshots are qualitatively similar to those obtained by Garaud & Kulenthirarajah (2016) in the non-rotating case. As the Richardson number increases from $Ri_F = 1$ (left-hand panel) to what Garaud & Kulenthirarajah (2016) refer to as the strongly stratified limit ($Ri_F =$ 100, centre panel), Fig. 6 shows that the scale of vertical velocity fluctuations decreases significantly. As discussed by Zahn (1992) (see also Garaud et al. 2017), the typical size of vertical eddies in non-rotating low Péclet number stratified turbulence is controlled by a combination of stratification and thermal diffusion, and would be proportional to $(Ri_{\rm eff}Pe_{\rm eff})^{-1/2}$ in the model set-up and nondimensionalization used here. This scaling is qualitatively consistent with the decrease in eddy size observed in the snapshots. Since a smaller eddy scale implies a decrease in the turbulent viscosity, this in turn results in a substantial increase of the amplitude of the mean flow, which is clearly seen in Fig. 5.

This somewhat simplistic discussion is, however, called into question if we look at the corresponding trajectories of these two simulations in Fig. 4. We see that they both lie close to the boundary between GSF-dominated and shear-dominated regimes, and in the case of the $Ri_F = 100$ simulation (aquamarine colour), both maps actually suggest that it lies in the GSF region of parameter space. An alternative explanation for the small eddy size observed in this simulation could then naively be that it is undergoing GSF-driven turbulence instead. But that interpretation is immediately invalidated by the presence of turbulence in regions of positive shear. In short, this example demonstrates the difficulty of identifying, simply from the position of the simulation on the linear stability maps, or from snapshots of \check{w} , whether the turbulence is shear-driven or GSF-driven. We will revisit this topic below in Section 6, where we will finally understand this particular simulation as one that is dominated by the non-linear branch of the shear instability.

Beyond a certain threshold in Ri_F , the dynamics change dramatically and become governed by almost 2D GSF modes when $Ri_F = 10\,000$ (bottom right panel in Figs 5 and 6). This result is relatively easy to understand given the position of the solution in the regime map (see the bottom right blue point in Fig. 4, top row): at these parameters, the shear instability is not linearly excited, and the GSF instability is very close to the marginal stability boundary and therefore barely supercritical. This likely explains why the modes do not become fully turbulent and, as we shall demonstrate in Section 6.6, why the non-linear shear instability is not triggered.

A similar transition between shear-dominated dynamics at low Richardson number and GSF-dominated dynamics at higher Richardson number is observed when the rotation rate is a little higher (middle row in Figs 5 and 6), i.e. when $Ro_F^{-1} = 1$. However, there are also a few important differences with the more weakly rotating case discussed above. In the leftmost panel of Fig. 6 (at Ri_F = 1), we see that the increased rotation rate causes the turbulence to be more coherent along the rotation axis. In the middle panel of the same row ($Ri_F = 100$, $Ro_F^{-1} = 1$), we see that the turbulence is becoming more inhomogeneous, somewhat suppressed in regions of positive shear, and enhanced in regions of negative shear (middle of the domain). In the rightmost panel of Fig. 6, the system is now clearly dominated by the GSF instability. The turbulence has a very small vertical scale, and is limited to the region of negative shear. This strong inhomogeneity leads to a notable asymmetry in the mean flow, for the reasons discussed in Section 5.3. This is illustrated in Fig. 7 which shows, for each of the simulations of Figs 5 and 6, a series of individual profiles of $u(\xi, t)$, for various times t selected once the system is in the statistically stationary phase. The layout is the same as in Figs 5 and 6. We see that all simulations that are clearly dominated by the GSF instability have asymmetric mean flow profiles with a weaker negative shear in the turbulent

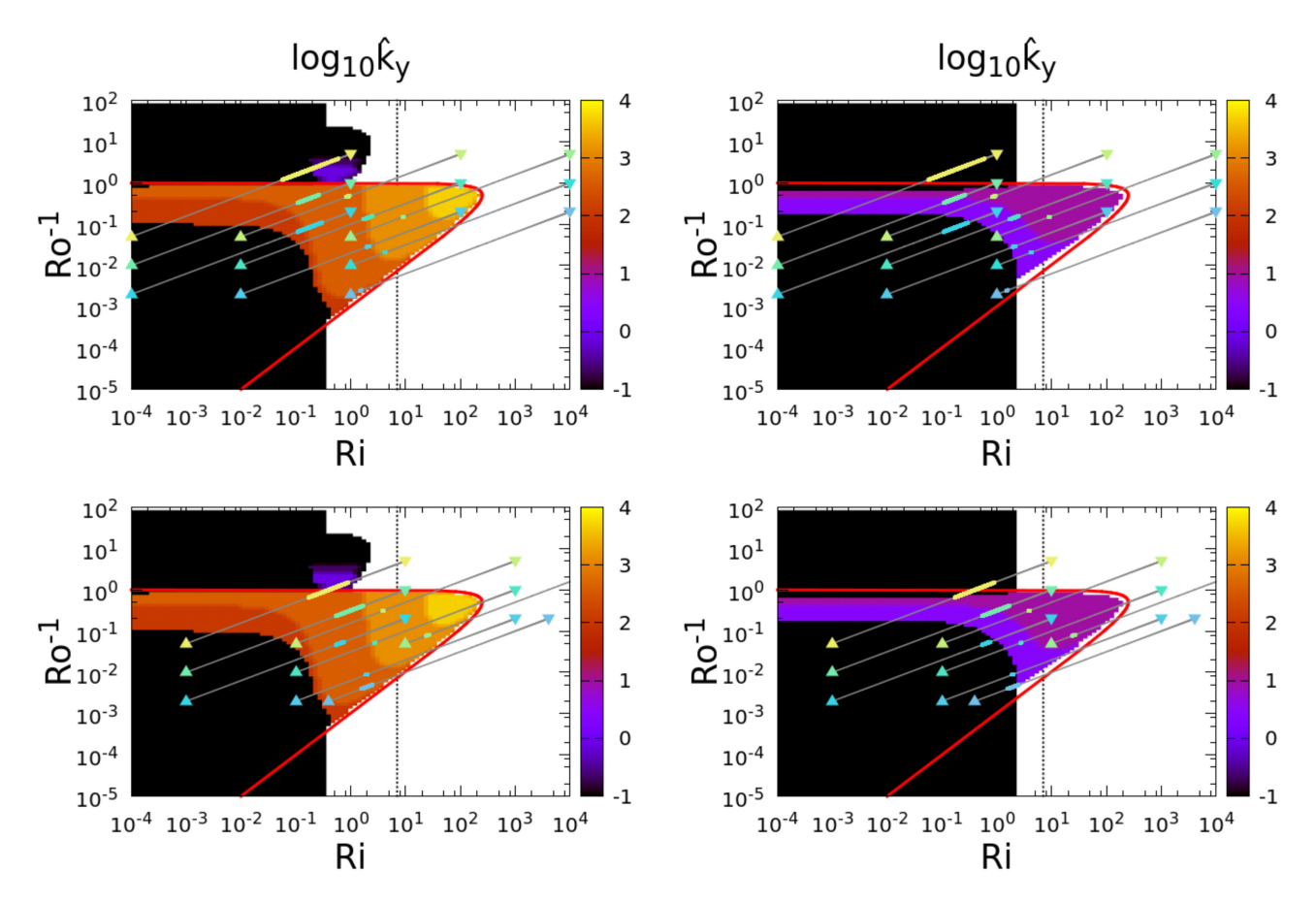


Figure 4. Effective parameters of a simulation plotted over the linear stability maps computed with Pe = 10, $Re = 10\,000$ (left) and $Pe_F = 0.1$, $Re_F = 100$ (right). The top row corresponds to the simulations discussed in Section 5, while the bottom row shows other available simulations (see Table 1). The upward and inverted triangles denote the position in parameter space of the laminar solution ($Ri_{eff} = Ri$, $Ro_{eff}^{-1} = Ro^{-1}$) and the fully turbulent solution ($Ri_{eff} = Ri_F$, $Ro_{eff}^{-1} = Ro_F^{-1}$) for each simulation, respectively. The thin grey line connecting an upward triangle to the inverted triangle of the same colour represents the maximum possible extent of a trajectory (see Section 5.3). The thicker coloured line overlaid on the grey line is the actual extent of the trajectory during the statistically steady state of the particular simulation.

region, and a stronger positive shear in the laminar regions, as in Fig. 3(b).

As we increase the rotation rate even further (top row in Figs 5–7), the effect of rotation on the shear-dominated regime becomes quite pronounced. The more weakly stratified simulation ($Ri_F = 1$) now shows roll-like structures that are invariant in the *y*-direction. This reduction of the flow dynamics to two dimensions reverses the sign of the energy cascade, and the shear-induced rolls now span the entire vertical height of the domain as well. The mean flow profile in this regime is highly variable, as seen in Fig. 7 (e.g. top left panel). However, this is only true at low Ri_F , and as the stratification increases, the flow becomes 3D again and transitions to GSF-dominated dynamics.

To summarize our findings so far, at least from a qualitative point of view, we have found that the dynamics appear to be either sheardominated or GSF-dominated depending on the parameters selected. This identification is sometimes trivial, as is the case for instance when the turbulence spans the entire domain (which would not happen in a GSF-dominated system), or in the case where the flow is invariant in the streamwise direction (which cannot extract any energy from the shear, and therefore could not be a shear instability). In other cases, by contrast, the identification can be much more difficult. We now turn to a quantitative analysis of momentum transport in our model system which, as we demonstrate below,

provides a useful and more systematic way of characterizing the dynamics of a simulation.

6 QUANTITATIVE ANALYSIS

6.1 Computing the turbulent viscosity

Assuming a linear relationship between the turbulent stress $\overline{\check{u}\check{w}}$ and the shearing rate $d\dot{\bar{u}}/d\dot{z}$ (see equation 38), we can compute the turbulent viscosity $\check{\nu}_{\text{turb}}$ by measuring $\overline{\check{u}\check{w}}$ and $d\check{\bar{u}}/d\check{z}$ from the DNS. We focus on the region near the middle of the domain where the shear is negative (so both instabilities can be present) and relatively constant. We therefore restrict our measurements to the interval $\check{z} \in [\pi - 0.5, \pi + 0.5]$. For each simulation, we take all profiles of $d\tilde{u}/d\tilde{z}$ that were saved during the statistically stationary state, and fit a constant to these profiles in the interval considered. The measured mean shearing rate is then denoted \check{S}_{mid} and the standard deviation around the mean yields an estimate of the measurement error and/or its variability. Similarly, we take all available profiles of $\check{u}\check{w}$ during the statistically stationary state, and fit a constant to these profiles in the same interval. The measured mean stress is denoted $(\check{u}\check{w})_{mid}$, and its standard deviation is used to estimate the measurement error/variability. Both procedures are illustrated in Fig. 8, for the simulation with parameters $Ro_F^{-1} = 1$ and $Ri_F = 100$.

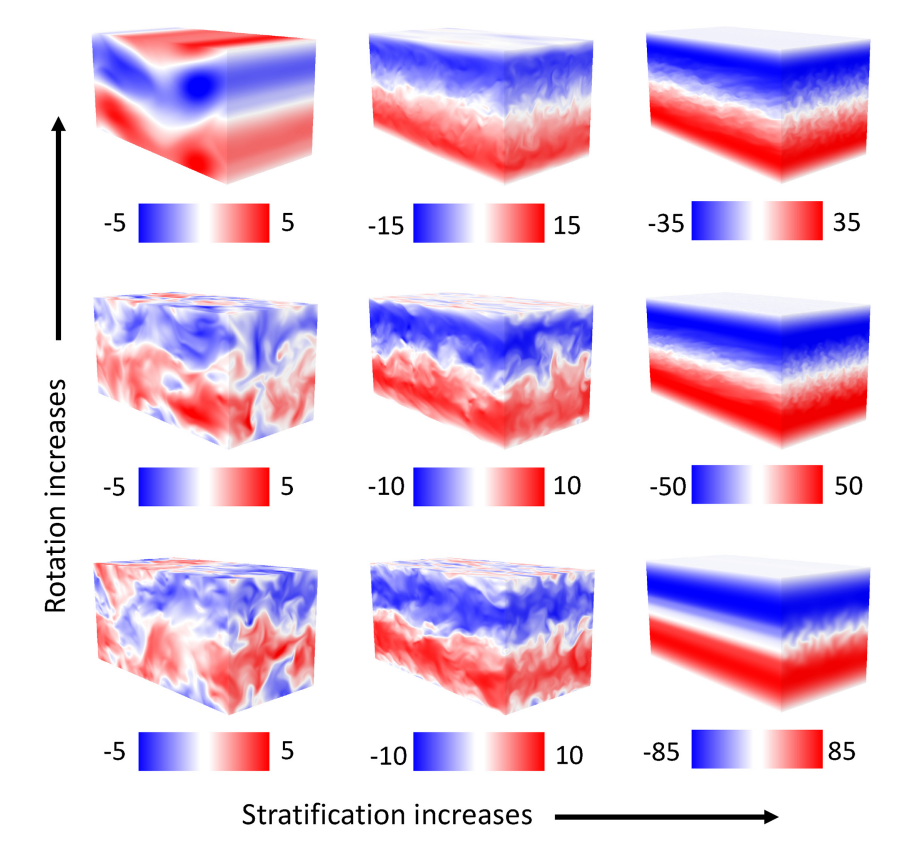


Figure 5. Representative snapshots of \check{u} from simulation data for $Re_F = 100$, $Pe_F = 0.1$ ($Re = 10^4$, Pe = 10). From top to bottom: $Ro_F^{-1} = 5$, 1, 0.2 ($Ro^{-1} = 0.05$, 0.01, 0.002). From left to right: $Ri_F = 1$, 100, 10 000 (Ri = 0.0001, 0.01, 1). In each snapshot, the long side of the domain corresponds to the streamwise direction (x), the vertical (z) is aligned with that of the page, and the remaining direction is that of the rotation axis (y).

From these measurements, we deduce the non-dimensional value of the turbulent viscosity in the middle of the domain, as

$$\check{\nu}_{\text{turb}} = -\frac{(\check{u}\check{w})_{\text{mid}}}{\check{S}_{\text{mid}}}.$$
(45)

We can then compare our simulation data to the predictions of existing models, specifically those of Garaud et al. (2017) for the turbulent viscosity of non-rotating low Péclet number shear flows, and of Barker et al. (2019) for the turbulent viscosity induced by the GSF instability.

$6.2\,$ Comparison with the shear instability model of Garaud et al. (2017)

The model of Garaud et al. (2017) provides the following estimate² for the dimensional turbulent viscosity v_{turb} in non-rotating, stratified shear flows at low input Péclet number Pe_F:

$$\nu_{\text{turb}} = \frac{C}{1 + a(J\text{Pe}_F)^{-1}} \left(1 - \frac{J\text{Pr}}{(J\text{Pr})_c} \right)^b \frac{\kappa_{\text{T}}}{J} \quad \text{for } J\text{Pr} < (J\text{Pr})_c,$$
(46)

where J is the local Richardson number (which here is equal to Ri_F/\check{S}_{mid}^2), Pr is the Prandtl number (which is equal to 0.001 in our

DNS), and where $C \approx a \approx 0.08$, $b \approx 0.25$, and $(JPr)_c \approx 0.007$ are model constants that were fitted to the non-rotating data (see Garaud et al. 2017). Non-dimensionally, this becomes

$$\tilde{\mathbf{v}}_{\text{turb}} = \frac{C}{a + J \text{Pe}_F} \left(1 - \frac{J \text{Pr}}{(J \text{Pr})_c} \right)^b \quad \text{for } J \text{Pr} < (J \text{Pr})_c,$$
(47)

which tends to $C/a \simeq 1$ as $J \to 0$. This is expected from the non-dimensionalization selected, which assumes a balance between the turbulent stresses and the forcing.

Fig. 9(a) shows the quantity $\check{\nu}_{turb}$ computed from the DNS in the manner described in the previous section, as a function of JPr. It is compared with the model prediction (magenta curve, which represents the right-hand side of equation 47). Note that since $JPe_F =$ $JPrRe_F$, with $Re_F = 100$ being held constant, the right-hand side of this equation is a function of JPr only in our data set, hence our choice to present the results as a function of this quantity. Plotted in this manner, all simulations dominated by the shear instability should lie on (or close to) the magenta curve. The non-rotating DNS from Garaud & Kulenthirarajah (2016), which were run at the same values of Re_F and Pe_F as our rotating simulations, are shown as small solid grey circles. We see that the model fits these non-rotating simulations well, as expected, except for a little dip near $JPr \sim 0.001$, which seems to be a real feature of the data (see Garaud et al. 2017). Simulations for increasing rotation rates are shown as coloured circles (see legend for detail), and the size of the circle is linearly related to $-\log_{10}(Ri_F)$ (so the largest circles correspond to the least stratified simulations at $Ri_F = 1$, and the smallest circles correspond to the most strongly stratified simulations). The data reveal very interesting, if sometimes puzzling trends.

²On further inspection, we discovered that the formula given in equation (42) of Garaud et al. (2017) is actually not quite correct, using $(JPe)^{-1}$ in the denominator of the first term instead of $(JPe_F)^{-1}$. The formula provided here corrects this error. The constant a needed to be re-fitted accordingly.

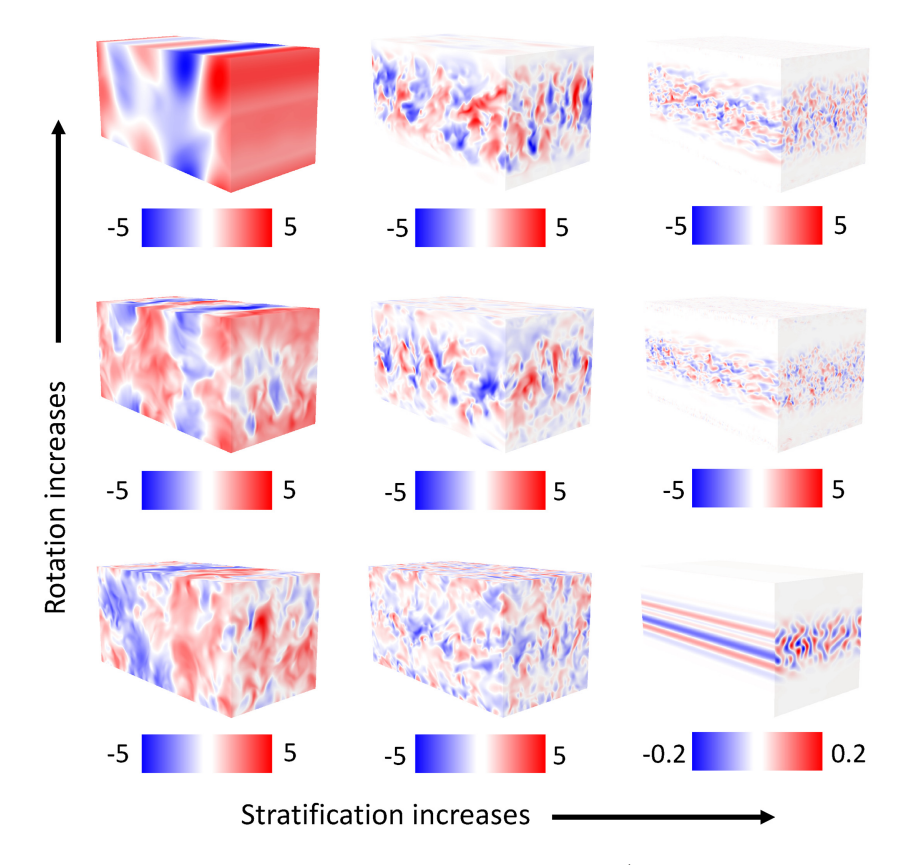


Figure 6. Representative snapshots of \check{w} from simulation data for $Re_F = 100$, $Pe_F = 0.1$ ($Re = 10^4$, Pe = 10). From top to bottom: $Ro_F^{-1} = 5$, 1, 0.2 ($Ro^{-1} = 0.05$, 0.01, 0.002). From left to right: $Ri_F = 1$, 100, 10 000 (Ri = 0.0001, 0.01, 1). The orientation of the domain is the same as in Fig. 5.

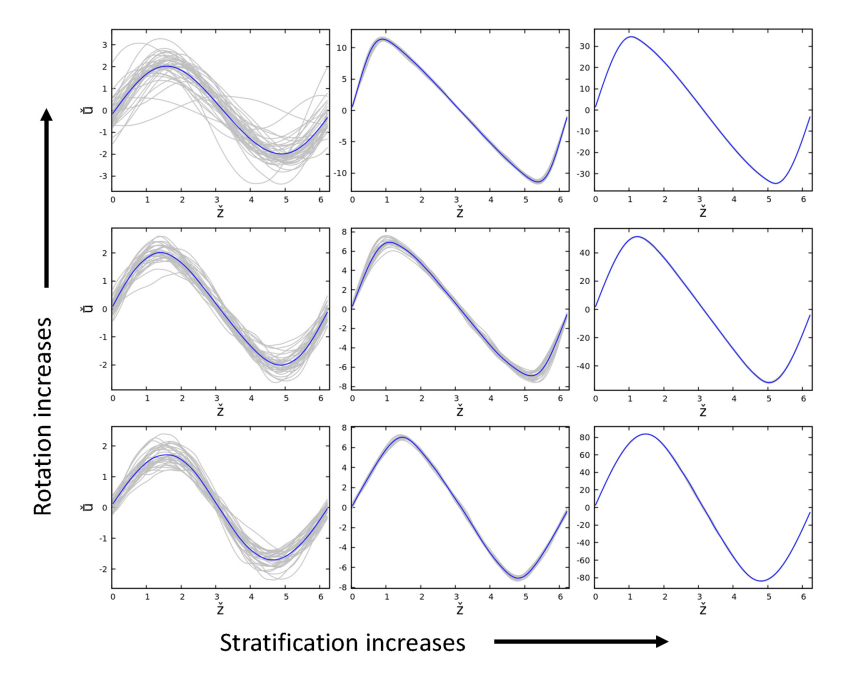


Figure 7. Horizontally averaged profiles of the mean flow $\check{u}(z,t)$ at selected instants in time, taken during the statistically stationary state, for $Re_F = 100$, $Pe_F = 0.1$ ($Re = 10^4$, Pe = 10). Instantaneous profiles are shown in grey, and their time average is shown in blue. From top to bottom: $Ro_F^{-1} = 5$, 1, 0.2 ($Ro^{-1} = 0.05$, 0.01, 0.002). From left to right: $Ri_F = 1$, 100, 10 000 (Ri = 0.0001, 0.01, 1).

6.3 Slowly rotating diffusive shear flows

As expected, most of the slowly rotating simulations ($Ro_F^{-1} = 0.2$, blue circles) lie close to the non-rotating data and the magenta model curve. We also see a few outliers, which have $Ri_F = 4000$ and 10

000, respectively, that turn out to be particularly interesting (see Section 6.6 below). Ignoring these outliers for now, our results tentatively confirm that turbulent transport for $\mathrm{Ro}_F^{-1}=0.2$ (and lower) is primarily shear-driven, and is consistent with the fact that

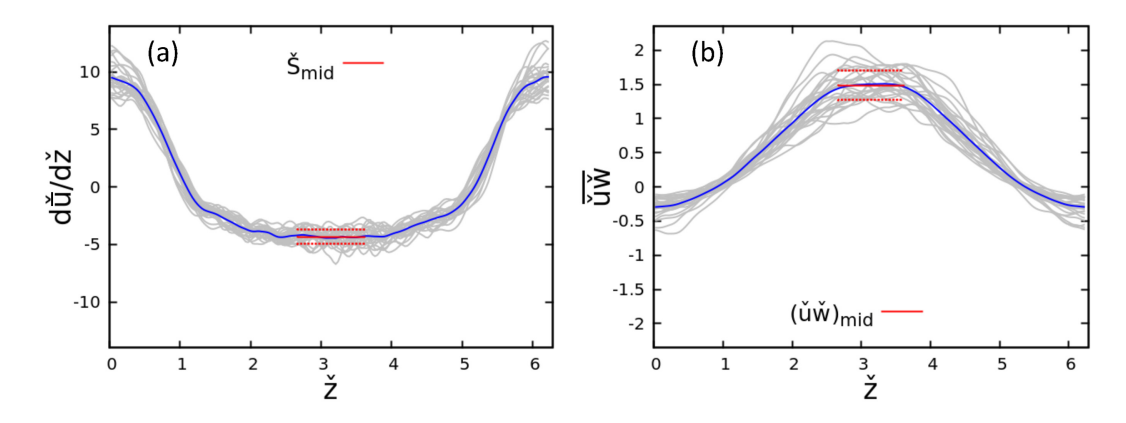


Figure 8. Illustration of data extraction method. Instantaneous profiles of $d\check{u}/d\check{z}$ and $\check{u}\check{w}$, extracted during the statistically steady state, are shown in grey, and their time average is shown in blue. We fit constants to these quantities in the interval $[\pi-0.5,\pi+0.5]$ to measure \check{S}_{mid} and $(\check{u}\check{w})_{mid}$. The extracted means are shown in the solid red line, and the dotted red lines are placed one standard deviation above and below. The parameters for this simulation are: $Ro_F^{-1}=1$ and $Ri_F=100$.

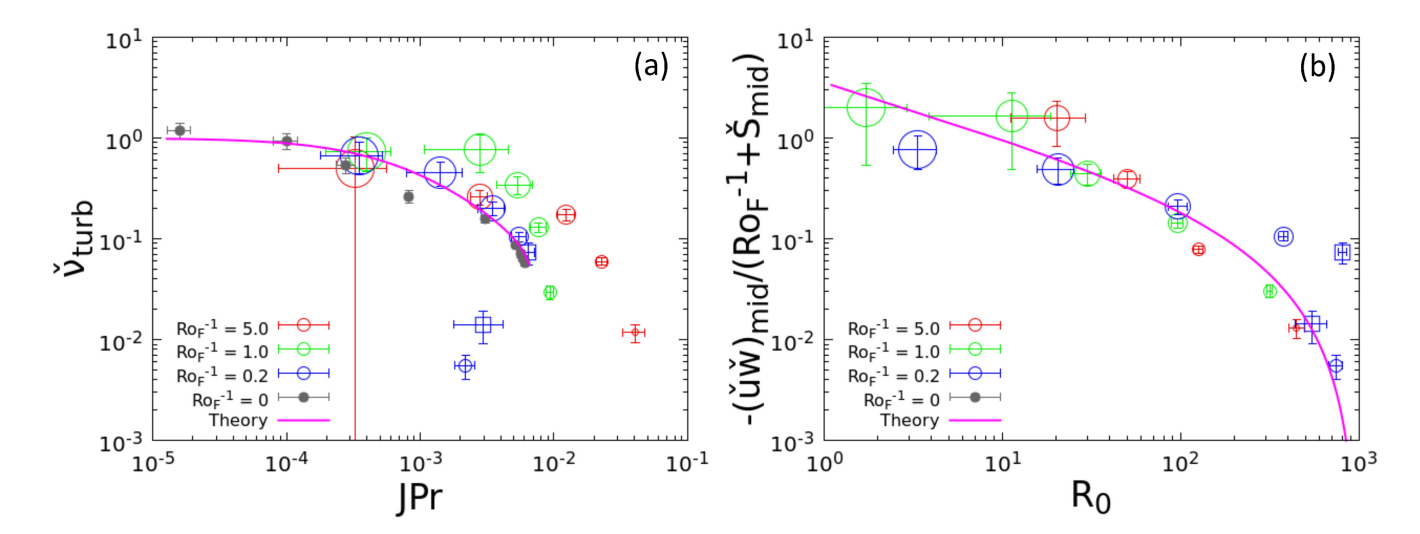


Figure 9. Comparison of \check{v}_{turb} and $(\check{u}\check{w})_{mid}$ (symbols) with the theoretical models (magenta lines) of Garaud et al. (2017) (left) and Barker et al. (2019) (right). The symbol colour represents the rotation rate (see legend) and the symbol size is inversely related to the stratification. The grey points are the non-rotating data of Garaud & Kulenthirarajah (2016). The square blue points correspond to a particular simulation at $Ri_F = 4000$ discussed in Section 6.7. Note the quantity plotted on the right-hand panel, $-(\check{u}\check{w})_{mid}/(Ro_F^{-1} + \check{S}_{mid})$ is essentially the same as \check{v}_{turb} when $Ro_F^{-1} \ll \check{S}_{mid}$.

the turbulence spans most of the computational domain (including, crucially, regions where the shear is positive) in the corresponding snapshots of Fig. 6.

However, it is important to note that, with the exception of the least stratified case (Ri_F = 1), the mean flow is *linearly stable* to the shear in these simulations. As such, the dynamics observed in simulations for Ri_F = 10, 100, and 1000 must be driven by *non-linear* shear instabilities. It is easy to verify that our findings are consistent with Zahn's instability criterion (see Zahn 1974; Garaud et al. 2017 and Section 1): indeed, the blue points all lie in the region where *J*Pr < (*J*Pr)_c \simeq 0.007. Interestingly, some of them get very close to this stability threshold, suggesting that weak rotation does not affect it.

In summary, we find that for weak rotation, and moderate stratification, existing models for turbulent mixing by diffusive stratified shear flows hold. The same is not true, however, for larger rotation rates and/or very strong stratification.

6.4 Comparison with the GSF instability model of Barker et al. (2019)

For more rapidly rotating simulations (higher Ro_F^{-1}), we see that, with a few exceptions at lower values of the stratification, the data do not fall on the model curve for shear-induced turbulence, and instead lies above it (most red and green points). This is not surprising since many of these simulations were tentatively identified as being GSF-dominated in the previous section. We do note that the GSF instability not only persists for JPr > 0.007 (which is not unreasonable, since it is not limited by Zahn's criterion), but can also have a turbulent viscosity that is sometimes substantially larger than that of the pure shear instability. To see why this is the case, we now compare our data with the GSF model of Barker et al. (2019).

Barker et al. (2019) studied turbulent transport by the GSF instability, and proposed a model for the turbulent viscosity at saturation

4928 E. Chang and P. Garaud

that relies on balancing the growth rates of primary instability and parasitic instabilities (see also Brown et al. 2013, for related work on the analogous fingering instability). Dimensionally, when written using the notation of this paper, their model predicts that the Reynolds stress should be

$$\overline{uw} = -C_B^2 \frac{S_{\text{mid}} + 2\Omega}{\lambda + \nu k_v^2} \frac{\lambda^2}{k_v^2},\tag{48}$$

where λ and k_y are the dimensional growth rate and wavenumber of the fastest-growing GSF mode, $S_{\rm mid}$ is the dimensional value of the shearing rate (taken here in the middle of our domain, where it is negative), and C_B is a constant of order unity that needs to be fitted to the data. Barker et al. (2019) find³ that $C_B \simeq \sqrt{8}$. We can express this in our code units to get a prediction for the Reynolds stress in the middle of the domain:

$$(\check{u}\check{w})_{\text{mid}} = -C_B^2(\check{S}_{\text{mid}} + \text{Ro}_F^{-1}) \frac{\check{\lambda}^2}{\check{k}_v^2(\check{\lambda} + \text{Re}_F^{-1}\check{k}_v^2)}.$$
 (49)

We know from the analogy between the GSF and the fingering instabilities, that when λ and k_y are written in the natural units for double-diffusive convection [namely, $d=(\kappa_T \nu/N^2)^{1/4}$ as the unit length, and d^2/κ_T as the unit time], they are only functions of the Prandtl number, and of the so-called equivalent density ratio, defined in our units as

$$R_0 = -\frac{\text{Ri}_F}{\text{Ro}_F^{-1}(\text{Ro}_F^{-1} + \check{S}_{\text{mid}})}$$
 (50)

(see Section 1). An alternative way of writing (49) is therefore

$$-\frac{(\check{u}\check{w})_{\text{mid}}}{\text{Ro}_F^{-1} + \check{S}_{\text{mid}}} = \frac{C_B^2}{\text{Pe}_F} \frac{\lambda_{\text{gsf}}^2}{k_{\text{gsf}}^2 (\lambda_{\text{gsf}} + \text{Pr}k_{\text{gsf}}^2)},$$
 (51)

where $\lambda_{\rm gsf}$ and $k_{\rm gsf}$ are the growth rate and wavenumber of the fastest-growing GSF modes expressed in their natural units (so $\lambda_{\rm gsf} = \lambda d^2/k_{\rm T}$ and $k_{\rm gsf} = dk_{\rm y}$). Using this expression has two advantages. First, note that the right-hand side of (51) is a function of R_0 only when the Prandtl number is fixed, which is the case of our simulations. As such, and as demonstrated by Barker et al. (2019), plotting the quantity $-(\check{u}\check{w})_{\rm mid}/({\rm Ro}_F^{-1}+\check{S}_{\rm mid})$ against R_0 should collapse the data on a single curve if the system is only subject to the GSF instability. Secondly, note that $-(\check{u}\check{w})_{\rm mid}/({\rm Ro}_F^{-1}+\check{S}_{\rm mid})\simeq -(\check{u}\check{w})_{\rm mid}/\check{S}_{\rm mid}\simeq\check{v}_{\rm turb}$ when ${\rm Ro}_F^{-1}\ll |\check{S}_{\rm mid}|$, which is often the case in our simulations. As a result, plotting $-(\check{u}\check{w})_{\rm mid}/({\rm Ro}_F^{-1}+\check{S}_{\rm mid})$ is almost the same as plotting $\check{v}_{\rm turb}$, which allows for an easy comparison with Fig. 9(a).

Fig. 9(b) shows $-(\check{u}\check{w})_{\text{mid}}/(Ro_F^{-1} + \check{S}_{\text{mid}})$ against R_0 computed using (50). The symbols used for each simulation are identical to the ones in Fig. 9(a), with the colour representing Ro_F^{-1} and the size representing Ri_F . The solid magenta line is the model prediction from equation (51), with the constant fitted to the data equal to $C_B \simeq \sqrt{8}$. Fig. 9(b) reveals a number of interesting features of our data.

First, note that not all simulations depicted in Fig. 9(a) are present in 9(b) – the largest red point, corresponding to a run with $Ro_F^{-1} = 5$, $Ri_F = 1$, is missing. This is because in this case, R_0 is smaller than one, and the system is not subject to GSF instabilities (consistent with the position of the simulation in the stability diagrams, see Fig. 4).

Secondly, looking at the remaining data points present in Fig. 9(b), we see that the turbulent viscosity model for the GSF instability provides a good explanation for the data in many, but crucially not

³More specifically, they find that a best fit to their data is obtained with $A \simeq 4$ (see their equation 31), which corresponds to $C_B \simeq \sqrt{8}$ using the relation $A^2/2 = C_R^2$.

all cases. In particular, we see a few blue points (for $Ro_F^{-1} = 0.2$) that clearly lie above the GSF model curve at large R_0 . These points correspond to those that are in the shear-unstable branch very close to JPr = 0.007 in Fig. 9(a), with $\tilde{v}_{turb} \simeq 0.1$. We therefore confirm that these simulations are dominated by the shear instability, and that the turbulent viscosity in that case is much larger than that of the GSF. Conversely, we now also see that the blue outliers that were lying well below the model curve for the shear instability in Fig. 9(a), are well explained by the GSF model curve in 9(b) (these are the blue points at very large R_0 that lie almost on top of the GSF model curve).

Finally, we were initially surprised to see that the GSF model curve fits the data for small R_0 quite well in Fig. 9(b), even when a simulation was identified to be in the shear-dominated regime. After further investigation, we discovered that this is most likely a coincidence that accidentally arose from our choice of parameters. Indeed, in the limit $R_0 \to 1$, one can use the asymptotic scalings derived by Brown et al. (2013) to show⁴ that $\lambda_{\rm gsf} \simeq \sqrt{\rm Pr}$ and $k_{\rm gsf} \simeq 1/\sqrt{2}$. With this, (51) implies that

$$-\frac{(\check{u}\check{w})_{\text{mid}}}{\text{Ro}_F^{-1} + \check{S}_{\text{mid}}} \simeq \check{v}_{\text{turb}} \simeq 2\frac{C_B^2}{\text{Pe}_F} \sqrt{\text{Pr}} \text{ when } R_0 \to 1, \text{ Pr} \ll 1, \quad (52)$$

(which is the case for our simulations, since Pr = 0.001). With $C_B^2 \simeq 8$, and $Pe_F = 0.1$, this predicts that $\tilde{\nu}_{turb} \simeq 5$ in weakly stratified systems which is quite close to what the shear instability model predicts in the same limit, but only coincidentally. Had we selected substantially different values of Pe_F or Pr, the GSF predictions and shear predictions would have been quite different, and we believe this would be more clearly visible in the data. As it is, we do see that the data at low R_0 is more consistent with being almost constant (which the shear model predicts) than with the GSF model, but this will need to be verified in the future with a more comprehensive exploration of parameter space.

6.5 Summary so far

To summarize our results, we find that the model of Barker et al. (2019) correctly predicts the turbulent viscosity measured in a simulation whenever it is dominated by the GSF instability. Similarly, the model of Garaud et al. (2017) correctly predicts the measured turbulent viscosity whenever a simulation is dominated by the shear instability. Taken on its own, this result is superficially pleasing but does not answer the more important question of when or why a simulation ends up being dominated by one instability or the other when both can theoretically be excited. A very naive approach would be to compare the linear growth rates of each mode of instability and select whichever is largest, but this would obviously not work here – in strongly stratified flows, the shear instability is primarily excited through a non-linear pathway, that cannot be captured in this manner. Ignoring the outliers (see below for more on these points), an alternative empirical answer to this question may be the following: the instability that ends up dominating is the one that would individually contribute the most to turbulent transport. In other words, one could compute the turbulent viscosity predicted by the GSF model of Barker et al. (2019), as well as the one predicted by the shear instability model of Garaud et al. (2017), and whichever one is the largest identifies the dominant instability. This method, when applied to our data, would correctly identify almost all simulations (and therefore also correctly predict the measured

⁴See equation B5 of Brown et al. (2013) using $\phi = 1$, because the equivalent of the diffusivity ratio τ is the Prandtl number for GSF modes.

turbulent viscosity), except for the outliers. It is therefore time to take a closer look at these simulations, to see what is happening in this case.

6.6 The outliers

The blue square and blue circle, found substantially below the magenta curve in Fig. 9(a), are from very strongly stratified simulations with $\mathrm{Ri}_F=4000$ and $\mathrm{Ri}_F=10~000$, respectively. These simulations are clearly GSF-dominated, despite satisfying Zahn's instability criterion ($J\mathrm{Pr}<0.007$), and despite the fact that at these parameters the model of Garaud et al. (2017) would predict a much larger turbulent viscosity than the model of Barker et al. (2019). This can be seen either from the individual snapshot in Fig. 6, which reveals the flow to be that of a 2D mode of the GSF instability, or from the corresponding position of the data points on Fig. 9(b), where they lie almost exactly on top of the GSF model curve. The existence of these points therefore appears to directly contradict the proposal made above to identify which instability ought to dominate.

More worryingly, they also show that it is possible to have two stratified rotating shear flows with similar values of JPr and the same rotation rate, but with two very different values of the turbulent viscosity – in the cases shown here, $\check{\nu}_{turb}$ in the GSF-dominated simulations is up to two orders of magnitude smaller than in the shear-dominated simulations at the same value of JPr and Ro_E^{-1} . Of course, it is important to remember that merely satisfying Zahn's instability criterion does not guarantee that a system will be subject to shear-induced turbulence. Since the instability is subcritical in that regime, its development relies on the availability of finiteamplitude perturbations of the right kind and of sufficient amplitude to 'prime' the turbulence. In the non-rotating case, as discussed in the introduction, this has been shown to lead to the existence of hysteresis in the system (Garaud et al. 2015; Garaud & Kulenthirarajah 2016; Gagnier & Garaud 2018), with otherwise similar simulations being turbulent or not depending on the manner in which they were initialized. It is therefore natural to find that the same phenomenon occurs in the rotating case, and the failure to trigger shear-induced turbulence in these outlying blue points is likely simply be due to the lack of a proper 'primer'. This realization brings us to the more interesting question of how to prime the non-linear shear instability.

6.7 Priming the shear instability

In the non-rotating case, priming the non-linear shear instability is quite difficult. Garaud & Kulenthirarajah (2016) and Garaud et al. (2017) were only able to do it by using as initial conditions the turbulent state of the system at a slightly lower stratification. In other words, the shear instability can persist into the non-linear regime if the stratification increases very gradually, but disappears otherwise. Interestingly, we are finding that the situation is quite different in the rotating case, because the GSF instability can serve as a primer for the shear instability, as long as it is not 2D.

A simple demonstration of this effect is shown in Fig. 10, which summarizes a simple experiment in which the Richardson number is suddenly increased at $\check{t} = \check{t}_{ref}$ from $Ri_F = 1000$ to $Ri_F = 1700$, in two simulations that had reached a statistically stationary shear-dominated state, one non-rotating (blue and magenta curves), and one at $Ro_F^{-1} = 0.2$ (red and green curves). We see that the turbulence, characterized for example by \check{w}_{rms} , dies out in the non-rotating case, but rapidly recovers in the rotating case, and remains at a level consistent with that of shear-induced turbulence. Since the rotating case is GSF unstable, we conclude that the small-scale turbulence

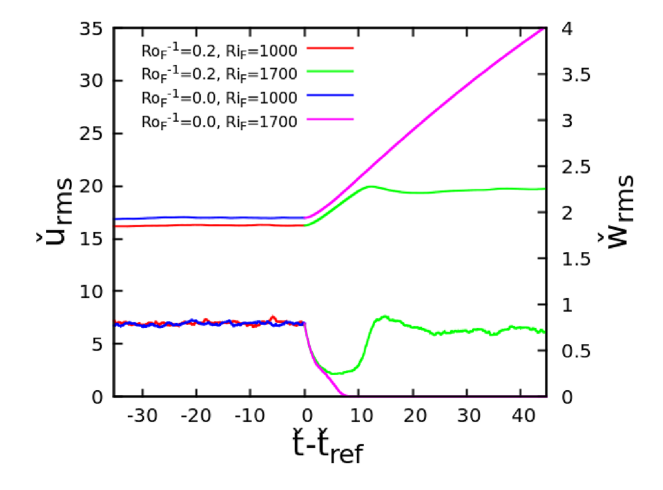


Figure 10. Illustration of the GSF instability's ability to prime the non-linear shear instability. The quantities \check{u}_{rms} (left axis, top curves) and \check{w}_{rms} (right axis, bottom curves) are shown for two simulations with $Ro_F^{-1} = 0$ (blue and pink curves) and 0.2 (red and green curves). At $\check{t} = \check{t}_{ref}$, the stratification increases from $Ri_F = 1000$ to $Ri_F = 1700$.

associated with the GSF instability must be able to prime the shear instability. In hindsight, this is not surprising. The GSF instability only exists because it is thermally diffusive (see Section 1), and therefore has a typical length-scale that is small enough for thermal diffusion to take place. This is precisely the characteristic eddy scale that is required to trigger the non-linear shear instability, and we see in this example that it does.

When the background stratification continues to increase, however, the system eventually approaches the marginal stability threshold for the GSF instability ($R_0 \rightarrow Pr^{-1}$, see equation 7). When this happens (e.g. for the simulation at $Ri_F = 10~000$, see Fig. 4), the saturated 'turbulent' state of the GSF remains 2D, and is invariant in the streamwise direction. Since it is not possible to extract energy from the shear using streamwise-invariant perturbations, this 2D form of the GSF instability cannot prime the shear instability, and the system remains in a GSF-dominated state. This explains the existence of the outliers discussed in Section 6.6, and why these are only found for very large R_0 .

Finally, we also found that the interaction of the shear instability and the GSF instability through priming can drive relaxation oscillations, a result that was fairly unexpected. These oscillations are illustrated in Fig. 11, which shows both \check{u}_{rms} and \check{w}_{rms} as a function of time, in a simulation at $Ro_F^{-1} = 0.2$, $Ri_F = 4000$. The horizontal axis shows $\check{t} - \check{t}_{ref}$, where \check{t}_{ref} in this case was arbitrarily selected to be the time origin once the system has entered this quasi-periodic state. The corresponding trajectory of this simulation on the stability map is shown in Fig. 4 (bottom row, bottom right blue/grey trace in each panel). The sequence of events associated with a single cycle of the oscillation (e.g. from $\check{t} - \check{t}_{ref} \simeq 10$ to 60 in Fig. 11) is as follows. At the start of the cycle, the system is in a state of weak shear, which is very close to being marginally stable to the GSF instability (near the red curve in Fig. 4). This state is unstable to a slowly growing, 2D GSF mode that eventually saturates (around $\check{t} - \check{t}_{ref} \simeq 25$). At this point, the flow looks like that of the bottom right panel of Figs 5 and 6. The system remains in that GSF-dominated state, but the background shear continues to increase in response to the forcing (albeit more slowly now). When the shear is large enough, the GSF flow becomes 3D, at which point the shear instability can finally be non-linearly excited (around $\check{t} - \check{t}_{ref} \simeq 40$). When this happens, the

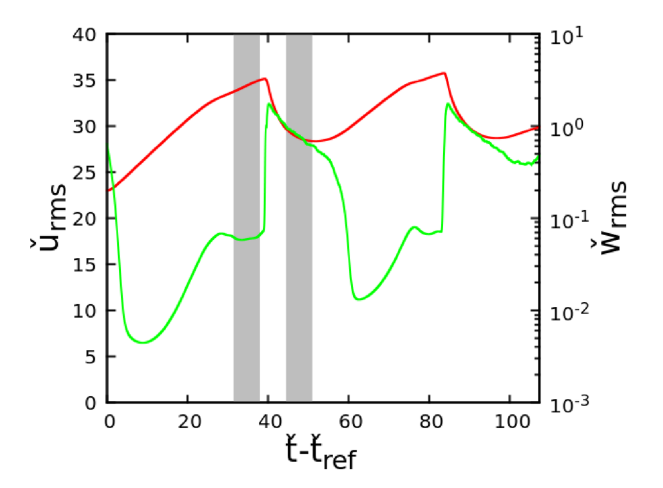


Figure 11. Illustration of relaxation oscillation dynamics that occur in a simulation at $Ro_F^{-1} = 0.2$ and $Ri_F = 4000$ (see text for detail), showing \check{u}_{rms} (left axis, red curve) and \check{w}_{rms} (right axis, green curve). The grey regions mark the two distinct time intervals over which the turbulent viscosity is measured, and shown as blue squares in Fig. 9.

flow looks like the bottom middle panel of Figs 5 and 6. The turbulent viscosity increases dramatically, and the shear decreases suddenly as a result. This happens too fast for the non-linear shear instability to keep up (even though JPr remains smaller than 0.007), and the latter dies down. The system moves back into the almost-marginally stable 2D GSF state, and the cycle repeats. This regular oscillation between a GSF-dominated state and a shear-dominated state can also be seen in Fig. 9. The square blue symbols both correspond to the same $Ri_F = 4000$ simulation discussed here, but were extracted during distinct time intervals, marked in grey in Fig. 11. We see that while the flow is shear-dominated the turbulent viscosity is relatively high and satisfies the Garaud et al. (2017) model, and when the flow is GSF-dominated the turbulent viscosity is low and satisfies the Barker et al. (2019) model.

This is an interesting example of a relaxation oscillation driven by the non-linear priming of one subcritical instability by another supercritical one. This oscillation between two turbulent states is accompanied by a significant oscillation in the mean flow amplitude. Assuming that these oscillations persist at lower Prandtl number, this mechanism could possibly be at the origin of shear oscillations in some stars that are close to the marginal stability threshold for the GSF instability.

7 SUMMARY AND DISCUSSION

In this work, we studied stably stratified, thermally diffusive, *rotating* shear flows in the equatorial region of stars, building on previous work that had focused on the non-rotating case (Prat & Ligniéres 2013; Garaud et al. 2015, 2017; Garaud & Kulenthirarajah 2016; Gagnier & Garaud 2018). This extension, as introduced in Section 1, is necessary since the main source of large-scale shear in stars is their differential rotation.

We used a very simple model set-up, in which a body force drives a vertically varying azimuthal flow (see Section 2). A linear stability analysis of this model (see Section 4) reveals the existence of two modes of instability: shearing modes, which only depend on the velocity gradient, and GSF modes, which only depend on the angular momentum gradient. Interestingly, both kinds of modes are found to coexist in a substantial region of parameter space in our model, which

naturally leads to the question of which instability dominates when both are excited. To complicate the matter further, diffusive shear instabilities are known to be non-linearly unstable (even when they are linearly stable), which means that they can coexist with the GSF instability in a much wider region of parameter space than what linear theory alone suggests.

Using DNS, we then studied the non-linear development of these instabilities, and were able to measure the turbulent viscosity they cause for a wide range of input parameters (varying both the rotation rate and the stratification). The limit of very low stratification, where the non-diffusive shear instability takes place, was briefly discussed for completeness, but is not particularly relevant for stellar interiors except perhaps very close to the edge of a convection zone where the buoyancy frequency drops to zero.

Much more relevant for stellar radiative zones is the limit of very large stratification (i.e. $Ri_F \gg 1$, see equation 34). A quantitative analysis of the simulation data for these cases showed that results in the weakly rotating limit (i.e. when the predicted Rossby number of the large-scale flow Ro_F defined in equation 34 is greater or equal to 5) are nearly identical to those of non-rotating simulations by Garaud & Kulenthirarajah (2016). In particular, we found that Zahn's non-linear instability criterion (Zahn 1974), namely JPr < (JPr)_c $\simeq 0.007$, still holds and that the model of Garaud et al. (2017) for mixing by diffusive turbulent shear flows (corrected for a minor error, see equation 46), correctly predicts the turbulent viscosity measured in the DNS when the shear instability is present. By contrast, the model of Barker et al. (2019) for the GSF instability would largely underpredict momentum transport for the same simulations. And yet, we also discovered that the shear instability is not necessarily always excited when $JPr < (JPr)_c$. This is a fundamental difference between linear and non-linear instabilities that should always be kept in mind - non-linear instabilities require a finite amplitude 'primer' of the right form to develop, otherwise the instability does not take place. When that is the case, the GSF instability dominates instead and the Barker et al. (2019) model correctly predicts the turbulent viscosity.

At larger rotation rates (i.e. for a predicted Rossby number Ro_F of order unity or less), the GSF instability is increasingly dominant, and the turbulent viscosity measured in the DNS is consistent with the Barker et al. (2019) model. At the same time, the shear instability does not appear to be active, but even if it were, the predicted turbulent viscosity from the shear model of Garaud et al. (2017) would be much smaller than that predicted by the GSF model of Barker et al. (2019), and would therefore be irrelevant.

These results pose an important question for stellar astrophysics. Indeed, stellar evolution codes usually compute turbulent mixing coefficients based on the local properties of the star (rotation rate, shear, stratification, etc.) - where local here means local both in space and time. When a single instability is present, the physics that need to be included in the construction of that turbulent mixing coefficient are usually clear (whether they are all taken into account is another matter of course). However, when multiple instabilities are present at the same time, as is the case here, we see that the answer is significantly less obvious. One could simply focus on the instability that has the largest linear growth rate and ignore the others. However, this procedure would ignore all subcritical instabilities (whose linear growth rate is zero or negative), and could potentially underestimate the true turbulent viscosity by orders of magnitude, as seen in Section 6.4. Ignoring potential interactions between the various instabilities, one could alternatively compute the turbulent viscosity associated with each of them individually (taking into account, this time, subcritical instabilities), and either add them all as is done in MESA for instance (Paxton et al. 2011), or take their maximum value.⁵ This approach is somewhat better supported by our data, but ignores the fact that subcritical instabilities are not always necessarily excited – see the discussion in Sections 6.6 and 6.7. This leads to the fundamental question of *how can we predict whether the non-linear shear instability is excited or not?*

On that particular matter, an interesting outcome of our investigation is the discovery that the GSF instability can serve as a primer for the shear instability, provided the former does not saturate into a purely 2D flow (see Section 6.7). In other words, the turbulence associated with the non-linear saturation of the GSF instability (which draws its energy from the unstable angular momentum gradient) can sometimes also tap into the shear itself, and further drive diffusive shear instabilities. To do so, the GSF flow must be fully 3D, which is usually the case unless R_0 defined in equation (9) is very close to the marginal stability threshold for the GSF (i.e. unless $R_0 \rightarrow Pr^{-1}$, see equation 7).

With this in mind, we now propose the following algorithm to model the turbulent viscosity when both GSF and shear instabilities are potentially present at the same time⁶: (1) Compute R_0 using (9), and if $1 < R_0 < \Pr^{-1}$ compute the associated turbulent viscosity for the GSF instability ν_{GSF} (using equation 10). (2) Compute JPr, and if JPr < 0.007 compute the turbulent viscosity associated with diffusive shear instabilities ν_{shear} (using equation 46). (3) If R_0 is close to \Pr^{-1} , the flow is likely 2D and will remain in a GSF state, hence use the computed value of the turbulent viscosity ν_{GSF} (based on the discussion in Section 6.6). (4) If R_0 is substantially lower than \Pr^{-1} , so the GSF instability is 3D, then let $\nu_{\text{turb}} = \max(\nu_{\text{shear}}, \nu_{\text{GSF}})$. This also identifies the dominant instability in the flow.

In this algorithm, the only missing ingredient is the threshold (in terms of R_0) beyond which the GSF instability remains 2D. Finding this threshold will require a better understanding of the non-linear saturation mechanism for the GSF instability at large R_0 . From the numerical experiments shown in this paper at Pr = 0.001, we found that the GSF flow stays 2D when R_0 exceeds about $500 = 0.5Pr^{-1}$ (see in particular Fig. 9b). Whether a similar rule applies when Pr is much smaller remains to be determined.

Of course, much more work remains to be done before one can gain a complete understanding of shear instabilities and GSF instabilities in stars. In particular, this study was limited to the equatorial region of a star, and the dynamics away from the equator are known to be substantially different, both for the GSF instability (Knobloch & Spruit 1982; Barker et al. 2020), and for the shear instability (Cope, Garaud & Caulfield 2020; Garaud 2020b). In the former case, Barker et al. (2020) found that the GSF instability criterion is relaxed compared with (5), and that angular momentum layering can lead to a vast increase in the turbulent transport coefficient. In the latter case, note that a star can undergo horizontal shear off equator, and Cope et al. (2020) and Garaud (2020b) found that the horizontal shear instability criterion is much less stringent than that of the vertical shear instability, and that transport can be quite efficient. As such, it is quite likely that most of our results do not apply at higher latitudes. In addition, most stars are magnetized, and the role of magnetic fields in suppressing or enhancing transport is highly non-trivial (see e.g. Tobias, Diamond & Hughes 2007; Harrington & Garaud 2019; Chen & Diamond 2020). Nevertheless, our study has shed light on what might happen when these two very different instabilities coexist, demonstrating that it can lead to a variety of interesting and, in the case of the relaxation oscillations, potentially observable phenomena.

ACKNOWLEDGEMENTS

The simulations were performed using the PADDI code kindly provided by Stephan Stellmach, on the Extreme Science and Engineering Discovery Environment (XSEDE) supercomputing facility Comet. This work is funded by the National Science Foundation under Grant AST-1814327. We thank the referee, Adrian Barker, for insightful questions and comments that greatly helped improve this manuscript.

DATA AVAILABILITY

The data published in this paper (table, figures) are available upon request to the first author.

REFERENCES

Aerts C., 2021, Rev. Mod. Phys., 93, 015001

Anagnost J. J., Desoer C. A., 1991, Circuits Syst. Signal Process., 10, 101

Balmforth N. J., Young Y.-N., 2002, J. Fluid Mech., 450, 131

Barker A. J., Jones C. A., Tobias S. M., 2019, MNRAS, 487, 1777

Barker A. J., Jones C. A., Tobias S. M., 2020, MNRAS, 495, 1468

Blass A., Tabak P., Verzicco R., Stevens R. J. A. M., Lohse D., 2021, J. Fluid Mech., 910, A37

Brown J. M., Garaud P., Stellmach S., 2013, ApJ, 768, 34

Chen C.-C., Diamond P. H., 2020, ApJ, 892, 24

Cope L., Garaud P., Caulfield C., 2020, J. Fluid Mech., 903, A1

Fricke K., 1968, Z. Astrophysik, 68, 317

Gagnier D., Garaud P., 2018, ApJ, 862, 36

Gallet B., 2015, J. Fluid Mech., 783, 412

Garaud P., 2018, Annu. Rev. Fluid Mech., 50, 275

Garaud P., 2020a, in Rieutord M., Baraffe I., Lebreton Y., eds, Multi-Dimensional Processes In Stellar Physics. Evry Schatzman School, EDP Sciences, p. 13

Garaud P., 2020b, ApJ, 901, 146

Garaud P., 2021, Phys. Rev. Fluids, 6, 030501

Garaud P., Kulenthirarajah L., 2016, ApJ, 821, 49

Garaud P., Gallet B., Bischoff T., 2015, Phys. Fluids, 27, 084104

Garaud P., Gagnier D., Verhoeven J., 2017, ApJ, 837, 133

Garaud P., Kumar A., Sridhar J., 2019, ApJ, 879, 60

Goldreich P., Schubert G., 1967, ApJ, 150, 571

Harrington P. Z., Garaud P., 2019, ApJ, 870, L5

Howard L. N., 1961, J. Fluid Mech., 10, 509

Hughes D. W., Weiss N. O., 1995, J. Fluid Mech., 301, 383

Høiland E., 1941, Klasse, 11, 1

Høiland E., 1939, Arch. Math. Naturv., 42, 25

Knobloch E., 1982, Geophys. Astrophys. Fluid Dyn., 22, 133

Knobloch E., Spruit H. C., 1982, A&A, 113, 261

Korycansky D. G., 1991, ApJ, 381, 515

Miles J. W., 1961, J. Fluid Mech., 10, 496

Moll R., Garaud P., 2017, ApJ, 834, 44

Paxton B., Bildsten L., Dotter A., Herwig F., Lesaffre P., Timmes F., 2011, ApJS, 192, 3

Pinsonneault M., 1997, ARA&A, 35, 557

Prat V., Ligniéres F., 2013, A&A, 551, L3

Prat V., Lignières F., 2014, A&A, 566, A110

Prat V., Guilet J., Viallet M., Müller E., 2016, A&A, 592, A59

Radko T., 2016, J. Fluid Mech., 805, 147

Rashid F. Q., Jones C. A., Tobias S. M., 2008, A&A, 488, 819

Rayleigh L., 1917, Proc. R. Soc. A, 93, 148

Richardson L. F., 1920, Proc. R. Soc. A, 97, 354

⁵This, in our opinion, makes somewhat more physical sense, as it assumes that one instability ends up dominating all the other ones. In practice, the difference is not too significant.

⁶Regions of positive angular momentum gradient, where the GSF is not excited, must be treated differently.

4932 E. Chang and P. Garaud

Solberg M., 1936, Union Geodesique et Geophisique Internationale VIeme Assemblee, Edinburg, 2, 66

Spiegel E. A., Veronis G., 1960, ApJ, 131, 442

Stellmach S., Traxler A., Garaud P., Brummell N., Radko T., 2011, J. Fluid Mech., 677, 554

Tobias S. M., Diamond P. H., Hughes D. W., 2007, ApJ, 667, L113

Townsend A. A., 1958, J. Fluid Mech., 4, 361

Traxler A., Garaud P., Stellmach S., 2011, ApJ, 728, L29

Zahn J.-P., 1974, in Ledoux P., Noels A., Rodgers A. W., eds, Stellar Instability and Evolution, Vol. 59, IAU Symp., p. 185Zahn J.-P., 1992, A & A, 265, 115

This paper has been typeset from a $T_EX/I^{\Delta}T_EX$ file prepared by the author.